21. Sonar Sensing

Lindsay Kleeman, Roman Kuc

Sonar or ultrasonic sensing uses the propagation of acoustic energy at higher frequencies than normal hearing to extract information from the environment. This chapter presents the fundamentals and physics of sonar sensing for object localization, landmark measurement and classification in robotics applications. The source of sonar artifacts is explained and how they can be dealt with. Different ultrasonic transducer technologies are outlined with their main characteristics highlighted.

Sonar systems are described that range in sophistication from low-cost threshold-based ranging modules to multitransducer multipulse configurations with associated signal processing requirements capable of accurate range and bearing measurement, interference rejection, motion compensation, and target classification. Continuous-transmission frequency-modulated (CTFM) systems are introduced and their ability to improve target sensitivity in the presence of noise is discussed. Various sonar ring designs that provide rapid surrounding environmental coverage are described in conjunction with mapping results. Finally the chapter ends with a discussion of biomimetic sonar, which draws inspiration from animals such as bats and dolphins.

Part C | 21

21.1 Sonar Principles

Sonar is a popular sensor in robotics that employs acoustic pulses and their echoes to measure the range to an

Fig. 21.1a–d Sonar ranging principles: **(a)** sonar configuration, **(b)** echo waveform, **(c)** range dot placement, **(d)** sonar map

Fig. 21.2a–c False range reading: **(a)** sonar configuration, **(b)** probing pulse 2 transmitted before echo from pulse 1 arrives, **(c)** false range (FR) is measured from transmission time 2

object. Since the sound speed is usually known, the object range is proportional to the echo travel time. At ultrasonic frequencies the sonar energy is concentrated in a beam, providing directional information in addition to range. Its popularity is due to its low cost, light weight, low power consumption, and low computational effort, compared to other ranging sensors. In some applications, such as in underwater and low-visibility environments, sonar is often the only viable sensing modality.

Sonars in robotics have three different, but related, purposes:

1. Obstacle avoidance: the first detected echo is assumed to measure the range to the closest object. Robots use this information to plan paths around obstacles and to prevent collisions.
2. Sonar mapping: a collection of echoes acquired by performing a rotational scan or from a sonar array is used to construct a map of the environment. Similar to a radar display, a range dot is placed at the detected range along the probing pulse direction.
3. Object recognition: a sequence of echoes or sonar maps is processed to classify echo-producing structures composed of one or more physical objects. When successful, this information is useful for robot registration or landmark navigation.
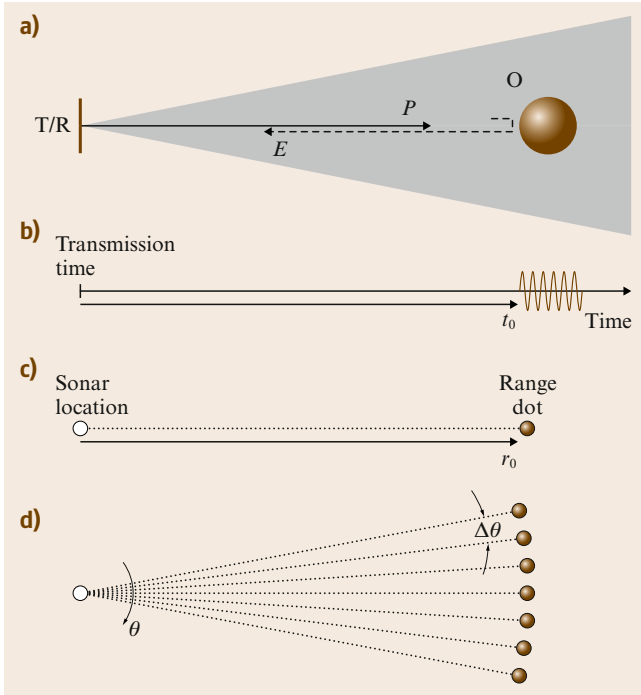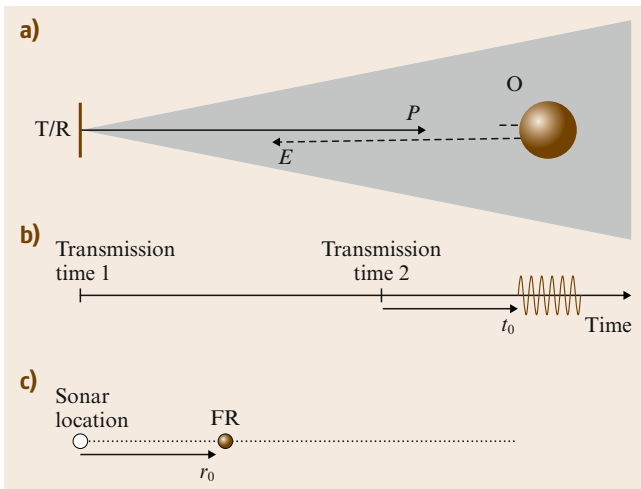
Figure 21.1 shows a simplified sonar system, from its configuration to the resulting sonar map. A sonar transducer, T/R, acts as both the transmitter (T) of a probing acoustic pulse (P) and the receiver of echoes (E). An object O lying within the sonar beam, indicated by the shaded region, reflects the probing pulse. A part of the reflected signal impinges on the transducer as is detected as an echo. The echo travel time t_0, commonly called the *time-of-flight* (TOF) is measured from the probing pulse transmission time. In this case the echo waveform is a replica of the probing pulse, which usually consists of as many as 16 cycles at the resonant frequency of the transducer. The object range r_0 is computed from t_0 using

$$r_0 = \frac{ct_0}{2} \, , \qquad (21.1)$$

where c is the sound speed (343 m/s at standard temperature and pressure). The factor of 2 converts the round-trip (P+E) travel distance to a range measurement. Beam-spreading losses and acoustic absorption limit sonar range.

In forming a sonar map, a range dot is placed along the direction corresponding to the transducer's physical orientation. A sonar map is usually built by rotating the sensor about the vertical axis, indicated by the orientation angle θ, through a series of discrete angles separated by $\Delta\theta$ and placing sonar dots the corresponding ranges. Since the range from the object O to the center of T/R is almost constant as T/R rotates, the range dots typically fall on a circle as long as O lies within the beam. Hence, sonar maps are made up of arcs.

The major limitations of sonar include

1. the wide sonar beam causes poor directional resolution. Objects are located at the middle of isolated arcs, but shorter-range objects shorten the arcs of those at farther ranges, and the arcs produced by a collection of objects are often difficult to interpret. A consequence of this effect is that wide beams occlude small openings, limiting robot navigation,

2. the slow sound speed, relative to an optical sensor, reduces the sonar sensing rate. A new probing pulse should be transmitted after all detectable echoes from the previous pulse have expired, otherwise the false reading shown in Fig. 21.2 can occur. The echo from probing pulse 1 occurs after probing pulse 2 is emitted. Sonar measures the TOF from the most recent probing pulse. Many sonars transmit probing pulses every 50 ms, but encounter false readings in reverberant environments,

3. smooth surfaces at oblique incidence do not produce detectable echoes. Figure 21.3 shows a planar surface (a wall) that acts as a mirror to the sonar beam. The important point is that the nearby wall does not itself produce a detectable echo, and a robot using sonar for obstacle avoidance may collide with the wall,

4. artifacts caused by beam side-lobes and multiple reflections produce range readings in the environment where no objects exist. Figure 21.3 also shows the redirected beam enclosing object O. The echo is also redirected by the wall back to the transducer. From the transducer's reference, the object is at the virtual object location VO, and it would generate the same sonar map as shown in Fig. 21.1. Since there is no physical object corresponding to the sonar dot location, it is an artifact. Also, note that the acoustic energy indicated by the dot-dashed line reflected back to the transducer is not detected because it does not lie within the beam cone. Beam side-lobes often detect these echoes and produce
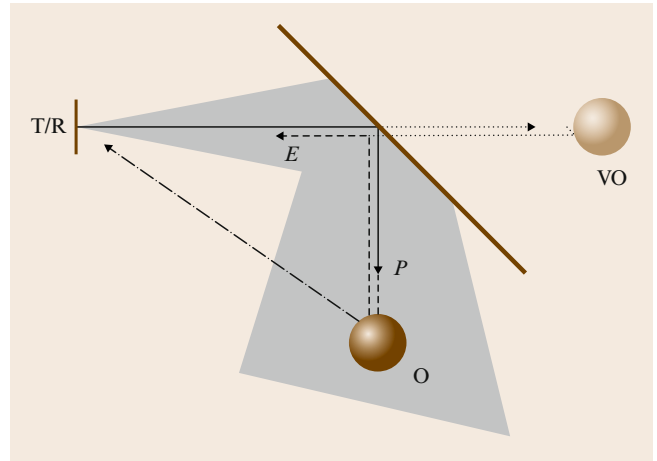
Fig. 21.3 The smooth surface redirects the beam, causing a sonar artifact at virtual object (VO) location. The *dot-dashed* echo path falls outside the sonar beam and does not produce a detectable echo
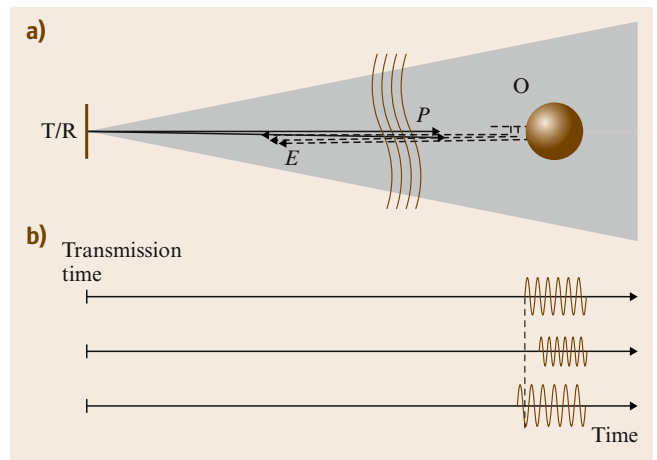
Fig. 21.4a,b Random echo jitter. (**a**) Sonar configuration; thermal inhomogeneities in the acoustic transmission medium cause refraction effects. (**b**) Examples of variations in echo travel times and amplitudes in a static environment

shorter-range readings but placed along the sonar orientation,

5. travel time and amplitude variations in the echoes caused by inhomogeneities in the sound speed. Both effects cause random fluctuations in the detected echo travel time, even in static environments. Figure 21.4 illustrates thermal fluctuations that cause speed up, retardation, and travel redirection by refraction of echoes. These cause temporal and amplitude variations in the echoes and jitter in the

range readings. While these typically introduce minor changes in sonar maps, they often cause havoc with approaches using finer analysis.

This chapter describes the physical and mathematical details that extend this simplified sonar model to practical sonar systems.

21.2 Sonar Beam Pattern

To derive a qualitative description of the sonar transducer, we apply elementary acoustics theory to a simplified model to achieve a simple analytic form [21.1]. A sonar emitter is commonly modeled as a circular piston surface of radius a vibrating with frequency f in an infinite planar baffle. The wavelength λ is

$$\lambda = \frac{c}{f} , \tag{21.2}$$

where c the sound speed in air, 343 m/s at 25 °C [21.2]. When $a > \lambda$ the emitted pressure field forms a beam consisting of a main lobe surrounded by side-lobes. In the far field, or range greater than a^2/λ, the beam is described by its *directivity pattern*, which is the two-dimensional Fourier transform of the aperture function, in this case the circular aperture produces a Bessel function. The emitted pressure amplitude at range r and angle θ relative to the piston axis can be written as

$$P_{\mathrm{E}}(r, \theta) = \frac{\alpha a^2 f}{r} \left(\frac{2 J_1(ka \sin \theta)}{ka \sin \theta} \right) , \tag{21.3}$$

where α is a proportionality constant that includes the density of air and the source strength, $k = 2\pi/\lambda$, and J_1 is the Bessel function of the first kind. The term in the brackets evaluates to 1 along the sonar axis, $\theta = 0$. The a^2 term indicates that the emitted pressure increases with the piston area. The frequency f appears in the numerator because the faster-moving piston generates higher pressures. The range r appears in the denominator because the conservation of energy requires the pressure to decrease as the beam widens with range.

The main lobe is defined by its first off-axis null, which occurs at an angle of

$$\theta_0 = \arcsin \left(\frac{0.61\lambda}{a} \right) = 14.7° . \tag{21.4}$$

For example, the popular electrostatic instrument grade transducer, formerly produced by Polaroid [21.3],

had a radius of $a = 1.8$ cm and is conventionally driven at $f = 49.4$ kHz, making $\lambda = 0.7$ cm and $\theta_0 = 14.7°$.

An object that is small compared to λ and located in the emitted pressure field produces an echo with a spherical wavefront whose amplitude decays with the inverse
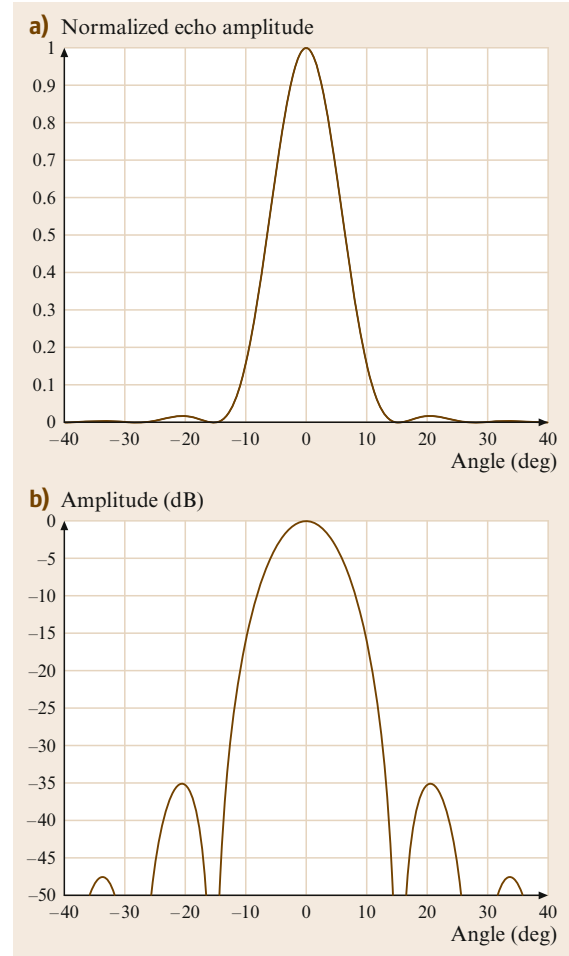

Fig. 21.5a,b Normalized amplitude of echo from small object predicted by the piston model as a function of angle. **(a)** Linear scale. **(b)** Decibel scale

of the distance propagated. In the common pulse-echo single transducer (*monostatic*) ranging sensor, only part of the echo wavefront impinges on the receiving aperture. The *sensitivity pattern* of the circular aperture, now acting as the receiver, has the same beam-like Bessel function form given in (21.3) by the reciprocity theorem [21.1]. If the reflecting object is located at (r, θ) relative to the transducer, the detected echo pressure amplitude, referenced to the receiver output, is given by

$$P_{\mathrm{D}}(r, \theta) = \frac{\beta f a^4}{r^2} \left(\frac{2J_1(ka \sin \theta)}{ka \sin \theta} \right)^2 , \qquad (21.5)$$

where β is a proportionality constant that includes parameters that cannot by controlled in a design, such as the density of air. The additional a^2 in the numerator occurs because larger apertures detect more of the echo wavefront.

Figure 21.5 shows the echo amplitude from a small (point-like) object located in the far field as a function of angle detected by the electrostatic instrument grade transducer. The curve has been normalized by the on-axis echo amplitude.

This model is qualitative in that it provides the following practically useful insights:

- For a small reflector size relative to the wavelength, the echo amplitude decreases inversely with the square of the range because there is a $1/r$ dispersion loss from the transmitter to the object, followed by an additional $1/r$ dispersion loss in the echo back to the receiver. However, larger reflectors can be treated using a Huygens principle approach [21.4] by dividing them into smaller reflectors and coherently adding their echo contributions. When this is done in two dimensions over a normally incident extended plane reflector, the echo amplitude decreases as $1/r$ rather than $1/r^2$. A cylindrical reflector extends over one dimension and results in an amplitude variation with range between $1/r$ and $1/r^2$. A more-extreme situation can occur with a concave reflector that acts as an acoustic magnifier, resulting in an amplitude that decreases with a negative power of range of less than one.
- The transducer excited by an approximation to a sinusoid exhibits side-lobes due to null caused by phase cancellation. For example, the 16-cycle excitation employed in the conventional sonar exhibits side-lobes. The peak of the first side-lobe is -35 dB relative to the echo amplitude when a small reflec-

tor lies on the transducer axis. The specification sheet for the 600 series instrument-grade transducer shows the first off-axis null at $15°$ and a first side-lobe peak magnitude of -26 dB. We presume that these measurements were made using a plane as a reflector.

- This model can be used to compute approximate beam parameter values for other common transducers. For example, the SensComp 7000 Series [21.5] with $a = 1.25$ cm yields $\theta = 20°$, equal to the specified value. However, the specified first side-lobe peak magnitude equals approximately -16 dB, which is substantially different from the expected -35 dB.

The limitations of the qualitative model include:

- Actual transducers only approximate pistons vibrating in an infinite planar baffle. The infinite baffle directs all the radiated sound pressure into the half-space in front of the transducer. Actual transducers radiate in all directions, but most of the acoustic energy is concentrated within the main lobe.
- All pulse-echo ranging sonars operate with finite-duration pulses rather than infinite-duration sinusoids. Several systems described below use pulses that are quite different from a sinusoidal excitation, either in duration or in form. These are commonly analyzed by computing the spectrum of the pulse and decomposing it into several sinusoidal frequencies, each having its own beam pattern. For example, the echo amplitude predictions above are reasonably accurate, including beam width and side-lobes, for the 16-cycle pulses. However, when impulse or swept-frequency excitations are used, the net beam profile becomes the superposition (of linear amplitudes) of the beam patterns produced by each frequency component in the excitation. Such broadband excitations do not exhibit nulls because the nulls formed by one frequency are filled in by main and side-lobes of beams produced by other frequencies.
- Most sonar transducers are encased in protective housings. The electrostatic instrument-grade transducer cover forms a mechanical filter that enhances the acoustic output at 49.4 kHz. The cases of other transducers may distort the transmitted field, but most form some type of directional beam.
- The model does not include frequency-dependent acoustic absorption of the transmission medium. These reduce the echo amplitudes predicted by the model.

The analytic model above is limited to simple configurations. With current computational power, transducers can be extended to those with arbitrary, even multiple, apertures and with various excitations. Waveforms of echoes from objects having arbitrary shapes can be simulated by using Huygens principle [21.4]. The transmitter, receiver, and object surfaces are broken up into two-dimensional surface arrays of emitting, reflecting, and detecting elements, using squares of dimension $< \lambda/5$ (the smaller the better, but taking longer). The impulse response of a given configuration is computed by as-suming an impulsive emission and superimposing the travel times along all possible paths from all transmitter elements to all object elements and then to all receiver elements. The temporal resolution should be $< (20 f_{max})^{-1}$, where f_{max} is the maximum frequency in the excitation. A $1\,\mu s$ resolution is adequate for a 16-cycle 49.4 kHz excitation. A much finer resolution ($< 0.1\,\mu s$) is required for an impulsive excitation. The echo waveform is then computed as the convolution of this impulse response with the actual transmitted pulse waveform [21.4].

21.3 Speed of Sound

The speed of sound c varies significantly with atmospheric temperature, pressure, and humidity and can be critical in determining the accuracy of a sonar system. This section outlines the relationship between c and these variables and is based on [21.6, 7].

The speed of sound in dry air at sea-level air density and one atmosphere pressure is given by

$$c_T = 20.05\sqrt{T_C + 273.16}\ \mathrm{ms}^{-1}\ , \tag{21.6}$$

where T_C is the temperature in degrees Celsius. Under most conditions (21.6) is accurate to within 1%. However, should the relative humidity be known, a better estimate can be made as

$$c_H = c_T + h_r\big[1.0059\times 10^{-3} \\ + 1.7776\times 10^{-7}(T_C + 17.78)^3\big]\ \mathrm{ms}^{-1}\ . \tag{21.7}$$

Equation (21.7) is accurate to within 0.1% for temperatures in the range -30–$43\,^\circ$C for most pressures at sea level. Should atmospheric pressure, p_s be known then the following expression can be used

$$c_P = 20.05\sqrt{\frac{T_C + 273.16}{1 - 3.79\times 10^{-3}(h_r p_{sat}/p_s)}}\ \mathrm{ms}^{-1}\ , \tag{21.8}$$

where the saturation pressure of air, p_{sat} is dependent on temperature as follows

$$\log_{10}\left(\frac{p_{sat}}{p_{s0}}\right) \\ = 10.796\left[1 - \left(\frac{T_{01}}{T}\right)\right] - 5.0281\log_{10}\left(\frac{T_{01}}{T}\right) \\ + 1.5047\times 10^{-4}\{1 - 10^{-8.2927[(T/T_{01})-1]}\} \\ + 0.42873\times 10^{-3}\{-1 + 10^{4.7696[1-(T_{01}/T)]}\} \\ - 2.2196\ , \tag{21.9}$$

p_{s0} is the reference atmospheric pressure of 101.325 kPa and T_{01} is the triple-point isotherm temperature with the exact value of 273.16 K.

21.4 Waveforms

Sonars employ a variety of waveforms, the most common types of which are shown in Fig. 21.6. Each waveform can be considered the echo from a normally incident plane. Waveforms are classified as being narrow- or wide-band depending on their spectral bandwidth. Narrow-band pulses provide superior detection performance in the presence of additive noise, while wide-band pulses provide better range resolution and do not have side-lobes.

Figure 21.6a shows the waveform produced by the Murata 40 kHz piezoelectric transducer excited by an eight-cycle 40 kHz square wave 40 V_{rms}. The Murata

Fig. 21.6a–d Common sonar pulse waveforms. **(a)** Murata 40 kHz transducer (narrow band). **(b)** Polaroid 600 electrostatic transducer excited with 16-cycle sinusoid at 49.4 kHz (6500 ranging module – narrow band). **(c)** Polaroi 600 electrostatic transducer excited with decreasing-frequency excitation signal (wide band). **(d)** Polaroid 600 electrostatic transducer excited with 10 μs 300 V pulse (wide band) ▶

sensor is small, lightweight, and efficient, but has an approximately 90° beam width. These transducers are used in monostatic, bistatic, and multiple transducer arrays [21.8, 9].

The next three waveforms were produced by the Polaroid 600 electrostatic transducer. Similar waveforms are generated by the smaller Polaroid 7000 transducer. Figure 21.6b shows the waveform produced by the 6500 ranging module. This ranging module with its 10 m range, low cost, and simple digital interface is a popular choice for implementing sonar arrays and rings. While the electrostatic transducer is inherently wide-band, with a usable frequency range from 10 to 120 kHz [21.10], narrow-band pulses are produced by exciting the transducer with 16 cycles at 49.4 kHz. Figure 21.6c illustrates a means to exploit the wide bandwidth of the Polaroid electrostatic transducer by exciting it with a decreasing-frequency square wave. Such frequency-sweep pulses are processed by a band of band-pass filters to extract the frequency dependence of reflecting objects. A correlation detector, also know as a matched filter, compresses swept-frequency pulses to improve range resolution. Longer-duration (100 ms) pulses are used in CTFM systems. Figure 21.6d shows a wide-band pulse when the excitation is a 10 μs-duration 300 V pulse. The metal protective mesh, which also acts as a mechanical filter resonant at 50 kHz, was removed by machining to achieve a usable bandwidth from 10 kHz to 120 kHz, with the peak occurring at 60 kHz. Such wide-band pulses are useful for object classification [21.10, 11]. These pulses have small amplitudes, limiting their range to 1 m or less.
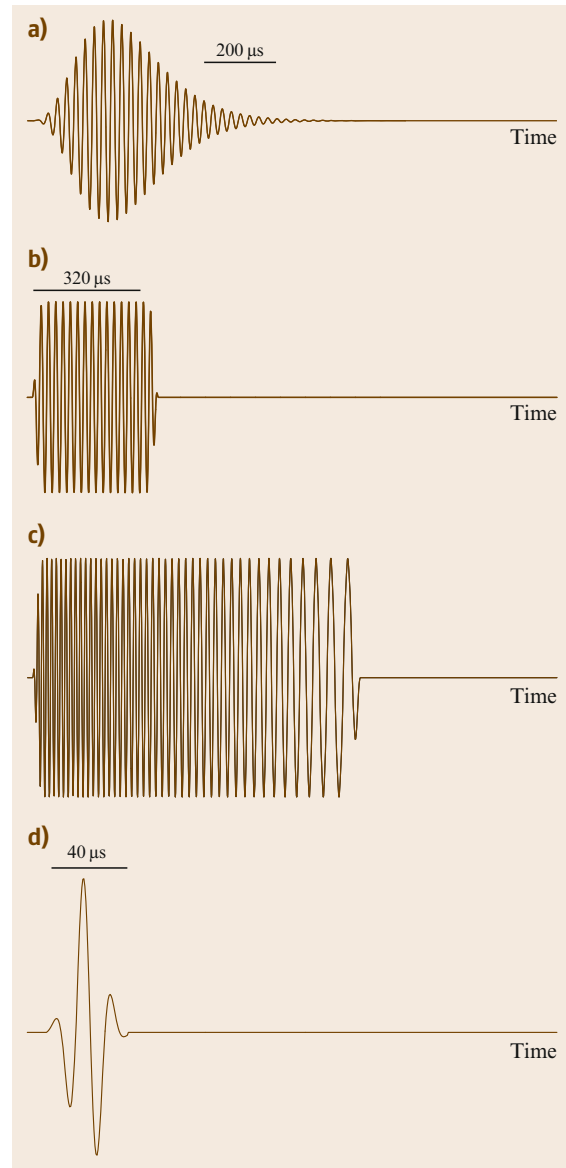
21.5 Transducer Technologies

Electrostatic and piezoelectric transducers are the two major types available that operate in air and can in principle operate both as a transmitter and receiver – some samples are shown in Fig. 21.7. In general electrostatic devices have a higher sensitivity and bandwidth but typ-

ically require a bias voltage above 100 V. Piezoelectric devices operate at lower voltages, making their electronic interfacing simpler, but have a high-Q resonant ceramic crystal and this results in a narrow frequency response compared to electrostatic transducers.

21.5.1 Electrostatic

An example of an electrostatic transducer is the Polaroid instrument-grade transducer (now available from SensComp.com) constructed from a gold-coated plastic foil membrane stretched across a round grooved aluminium back plate. The conductive foil is charged via a bias voltage of 150 V with respect to the back plate. Incoming sound waves vibrate the foil and change the average distance between the foil and back plate and thereby changing the capacitance of the foil. Assuming that the charge q is constant, the voltage $v(t)$ is generated proportional to this varying capacitance $C(t)$ as $v(t) = qC(t)$. As a transmitter, the transducer membrane is vibrated by applying $0-300$ V pulses across this capacitor, typically using a pulse transformer. The charge induced by the 300 V on the capacitor causes an electrostatic attraction force between the membrane and the back plate. The grooves on the back plate allow stretching of the membrane and by creating randomness in the back plate roughness a broad resonance can be achieved in the frequency response. For example the bandwidth of the 7000 series Polaroid transducer is 20 kHz. A front grille is mounted on the transducer and removing this grille reduces losses and reverberation between the grill and the membrane. Another electrostatic transducer was designed by Kay and details of its design can be found in [21.12].

21.5.2 Piezoelectric

Piezoelectric ceramic transducers can be used as both transmitters and receivers, however some manufacturers sell transmitters and receivers separately in order to optimize the transmitted power and receiver sensitivity,

respectively. A piezoelectric resonant crystal mechanically vibrates when a voltage is applied across the crystal, and in reverse generates a voltage when mechanically vibrated. Often a conical concave horn is mounted on the crystal to acoustically match the crystal acoustic impedance to that of air. An example is the Murata MA40A5R/S receiver and sender transducers, which operate at 40 kHz. This device has a diameter of 16 mm and a 60° beam angle for transmitter combined with receiver for -20 dB loss compared to the maximum sensitivity. The effective bandwidth of transmitter and receiver is only a few kHz due to the resonant nature of the crystals. This limits the envelope rise time of pulses to around 0.5 ms. An advantage is the ability to drive piezoelectric devices with low voltages, for example by connecting each terminal to complementary CMOS logic outputs. There is a wide range of resonant frequencies for piezoelectric transducers from 20 kHz to megahertz. Also available is piezoelectric film called polarized fluoropolymer, polyvinylidene fluoride (PVDF) from www.msiusa.com. This flexible film can be cut to shape and custom ultrasonic transmitters and receivers can be formed. The sensitivities of the transmitters and receivers made from PVDF is generally lower than that of ceramic crystal transducers and most applications are short range where the broadband nature of PVDF allows short pulses to be formed, allowing pulse-echo ranging to as little as 30 mm.

21.5.3 MEMS

Microelectromechanical system (MEMS) ultrasonic transducers can be fabricated on a silicon chip and integrated with electronics. The sensors offer a low-cost mass-produced alternative to standard transducers. MEMS ultrasonic transducers operate as electrostatic capacitive transducers where the membrane can be made from thin nitride. Devices operate at frequencies up to several megahertz and offer advantages in signal-to-noise ratio over piezoelectric devices due to their better matching to air acoustic impedance [21.13]. Two-dimensional arrays of devices can be deployed on a chip that are well matched and steerable.

21.6 Reflecting Object Models

Modeling the reflection processes helps in interpreting echo information. In this section we consider three simple reflector models: planes, corners, and edges, shown in Fig. 21.8. These models apply to both single transducers and arrays.

A plane is a smooth surface that acts as an acoustic mirror. Smooth walls and door surfaces act as planar reflectors. The plane must be sufficiently wide to produce the two reflections whose path is shown in dotted line. The plane reflector is then slightly larger than the intersection area of the beam with a plane of infinite extent. Smaller planes produces weaker echoes because of a smaller reflecting surface and negative interference by echoes diffracted from the edges of the plane. An acoustic mirror allows the analysis using a virtual transducer, indicated by primes in the figure.

A corner is the concave right-angle intersection of two surfaces. Corners formed by intersecting walls, the sides of file cabinets, and door jambs are commonly observed corner reflectors in indoor environments. The novel feature of the corner, and its three-dimensional (3-D) counterpart the corner cube, is that waves reflect back in the same direction from which they originate. This is caused by planar reflections at each of the two surfaces defining the corner. The virtual transducer is then obtained by reflecting the transducer about one plane of the corner and then the other plane. This gives rise to a reflection through the intersection point of the corner as shown in Fig. 21.8b. The virtual transducer analysis indicates that, for a monostatic sonar, echoes from a plane and corner are identical and that planes and corners can generate identical sonar maps [21.4]. The difference in the virtual transducer orientation between planes and corners has been exploited using transducer arrays to differentiate these reflectors [21.11, 14].

The edge shown in Fig. 21.8c models physical objects such as convex corners and high-curvature surfaces (posts), where the point of reflection is approximately independent of transducer position. Edges are encountered in hallways. While planes and corners generate strong echoes, edges generate weak echoes that are detected only a short range [21.4], making them difficult objects to detect. Early robot sonar researchers placed bubble wrap material on edge surfaces to make them reliably detectable.

Many environmental objects can be configured as a collection of planes, corners, and edges. Models for echo production [21.15, 16] indicate that normally incident surface patches and locations at which sharp changes in the surface function and its derivatives generate echoes. Objects with rough surfaces or a collection of many objects generate echoes from a variety of ranges and bearings, as illustrated in Fig. 21.9. If $p(t)$ repre-
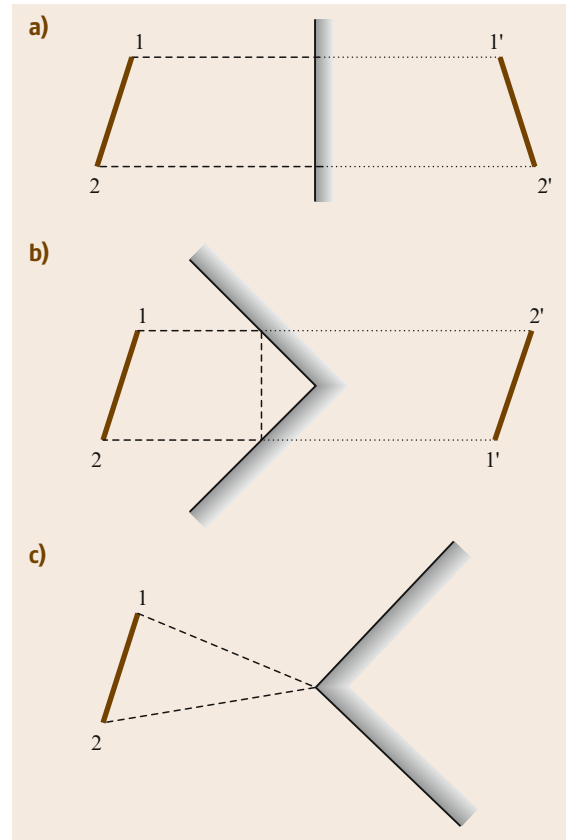

Fig. 21.8a–c Reflector models: **(a)** plane, **(b)** corner, and **(c)** edge
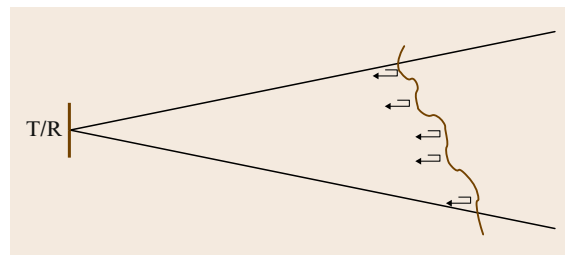

Fig. 21.9 Random reflector model. Echoes reflect back from normally incident surface sections within the beam

sents a single echo waveform, often a replica of the probing waveform, the total echo waveform $p_T(t)$ is the sum of individual echoes $p_i(t)$ from N normally incident patches at range r_i and bearing θ_i, scaled by amplitude a_i, or

$$p_T(t) = \sum_{i=1}^{N} a_i(\theta_i) p_i \left(t - \frac{2r_i}{c} \right) , \qquad (21.10)$$

where $a_i(\theta_i)$ is an amplitude factor related to the surface patch size and its bearing in the beam. Wide-bandwidth echoes are more complicated because their waveform changes in a deterministic fashion due to diffraction [21.11].

Sonars that analyze $p_T(t)$ employ analog-to-digital converters to obtain waveform samples [21.11, 17]. Reflecting patches separated in range produce isolated patches [21.11], but more often the incremental travel time is less than the pulse duration, causing pulse overlap. Rough surfaces and volume scatterers, such as indoor foliage, have large N, allowing $p_T(t)$ to be treated as a random process [21.18, 19]. Conventional TOF sonars output the first time that $p_T(t)$ exceeds a threshold [21.11].

21.7 Artifacts

Sonars usually work well in simple environments, while complex environments often produce mysterious readings, artifacts, that foil attempts to build reliable sonar maps. Artifacts have given sonar a bad reputation as being a noisy, or low-quality, sensing modality. Sonar stalwarts believe sonar would open up many new applications, *if only* we understood echoes at a level that approximates that employed by bats and dolphins [21.20]. Sonar stalwarts divide into two categories in terms of how they treat artifacts. The first attempts to build *intelligent sensors* that identify and suppresses artifacts before transmitting data to a higher-level reasoning program. Previous approaches [21.21, 22] required custom electronics, which other researchers have been reluctant to adopt because of expense or lack of experience. An alternate approach is to control conventional sonar in a novel fashion to produce a series of spikes and requires only software changes [21.23]. Sonar arrays have been used to find consistent data [21.24–26]. Echoes from specular reflectors, such as planes, corners, or posts, exhibit detectable features, which can be obscured by artifacts.

The second category of sonar users attempts to eliminate artifacts produced by conventional sensors by using higher-level postprocessing. These include proponents of occupancy (or certainty) grids [21.27, 28], including those that apply simplified physical models, such as sonar arcs [21.29, 30]. In simple environments postprocessing usually eliminates artifacts that are inconsistent with a feature [21.31] or with a physical map [21.30]. More-sophisticated methods handle artifacts by treating them as noise and applying hidden Markov models (HMM) [21.32]. However, multiple passes are needed to successfully teach the system about relatively simple environments, mostly because artifacts are not amenable

to being treated as independent additive noise. Eliminating troublesome artifacts would replace HMM with simpler Markov chains [21.33, 34], and sufficient sonar data can be obtained in a single pass. What frustrates this second category, and mildly amuses the first, is that this postprocessing works well *in simple environments*, but fails in real-world environments. This second category eventually abandons sonar and joins the camera and laser ranging crowd.

There are two important classes of artifacts: axial multiple reflection (MR) artifacts and dynamic artifacts. These artifacts are important in sonar mapping when they indicate the presence of a static object at a location where none exists. Troublesome MR artifacts are caused by delayed echoes produced by a previous probing pulse exceeding the detection threshold after the current probing pulse has been transmitted. Such artifacts then appear as close-range objects and obscure actual farther-range objects in conventional sonars. Most sonars employ probing pulse emission periods longer than 50 ms to avoid MR artifacts, although some reverberant environments can still produce artifacts [21.35].

Dynamic artifacts are produced by moving objects, such as individuals passing through the sonar beam. Even though these are actual objects and echoes indicate their true range, their presence should not be part of a sonar map that describes the static environment. Such dynamic artifacts make quantitative matchings between stored and generated sonar maps error-prone.

Another common artifact is a nonaxial MR artifact [21.4] caused by an obliquely incident smooth surface that redirects the sonar beam to some other echo-producing object. The TOF produces a range reading that is positioned along the sonar axis. While the object is

not at the location indicated on a sonar map, its location in the sonar map is a stable element and can be useful for navigation.

One may argue that, if the locations of all objects are known, the echoes can be determined and should not be treated as random processes. However, the presence of speed fluctuations in the medium due to thermal gradients and ever-present electronic noise cause random fluctuations in the times that thresholds are exceeded. Even a stationary sonar in a static environment exhibits random fluctuations [21.36], similar to the visual experience of fading when viewing objects beyond a heated surface.

Sonar can identify artifacts by applying three physical criteria that are met by echoes from static environmental objects. Artifact features include [21.35]

1. echo amplitude – echoes with amplitudes less than a specified threshold;
2. coherence – echoes forming constant-range azimuthal intervals less than a specified threshold; and
3. coincidence – echoes detected with a sonar array at different times (lacking temporal coherence) or corresponding to different locations (lacking spatial coherence).

21.8 TOF Ranging

Most conventional sonars employ Polaroid 6500 ranging modules [21.37] connected to the Polaroid 600 series electrostatic ultrasound transducer. The module is controlled with digital signals on two input lines (*INIT* for initialization and probing pulse transmission and *BLNK* for clearing the indication and resetting the detector) and the TOF reading occurs on its output line (*ECHO*). A logic transition on *INIT* causes the transducer to emit a pulse lasting for 16 cycles at 49.4 kHz. The same transducer detects echoes after a short delay to allow transmission transients to decay. Another interrogation pulse is typically emitted only after all the echoes produced by the previous pulse have decayed below a detection threshold.

The module processes echoes by performing rectification and lossy integration. Figure 21.10 illustrates a simulation of the processed waveform applied to the threshold detector. While the echo arrives at time t_0 after the emission, *ECHO* exhibits a transition at the measured TOF time t_m, the first time the processed echo signal exceeds a detection threshold τ. By convention, the range r of the reflecting object is calculated by

$$r = \frac{ct_m}{2} , \qquad (21.11)$$

where c is the speed of sound in air, usually taken as 343 m/s.

Figure 21.10b shows details around the threshold detection point including the residual high-frequency ripple after full-wave rectification and integration. Two effects can be noticed. First, t_m will always occur after t_0, making threshold detection a biased estimate of the true echo arrival time. Moreover, this bias is related to the echo amplitude: stronger echoes will produce an integrator output having a greater slope, which exceeds τ sooner than t_0. Second, as the echo amplitude decreases, for example, when the object moves away from the transducer axis, the threshold level occurs later in the integrator output and t_m will experience small jumps in time approximately equal to half the period [21.38].

The first step in developing a model of the detection process is to develop a model for the echo amplitude as a function of bearing. The Polaroid transducer is often modeled as a vibrating piston to yield the transmitter/receiver beam pattern shown in Fig. 21.11. To
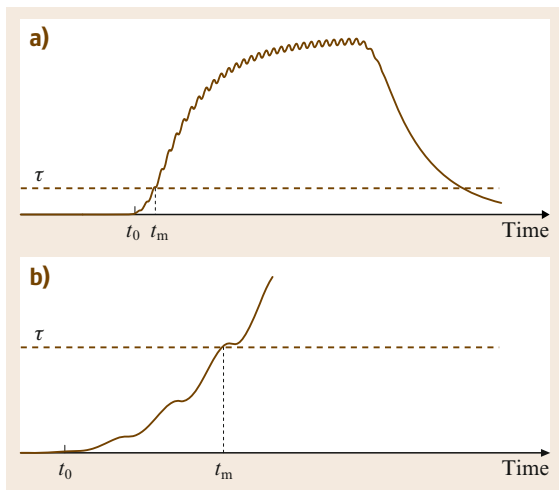

Fig. 21.10a,b Simulation of Polaroid ranging module operation. (**a**) Processed echo waveform. (**b**) Expanded time and amplitude scale around threshold crossing point
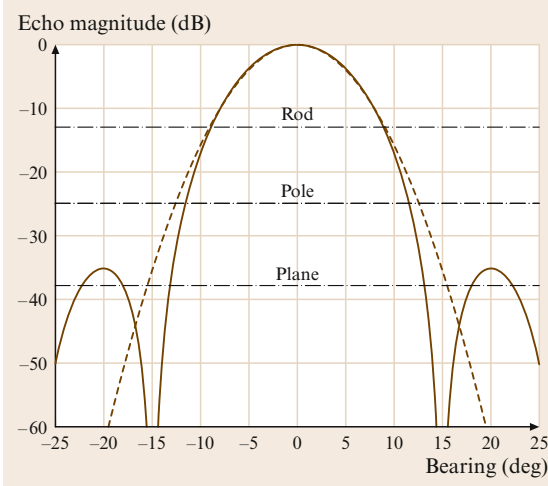
Fig. 21.11 Piston model transmitter/receiver pattern for the Polaroid 600 series transducer. A Gaussian approximation with SD $= 5.25°$ is shown in *dashed line*. Equivalent threshold levels for plane, pole, and rod objects at 1.5 m range are shown as *dot-dashed lines*
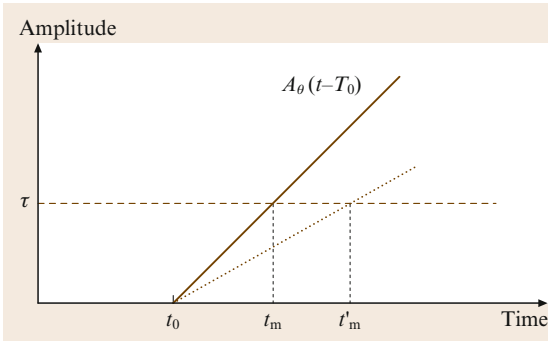
Fig. 21.12 TOF values t_m and t'_m for idealized processed echo waveforms having two amplitudes. The *solid line* indicates a larger-amplitude echo

Fig. 21.13a−c TOF data from an object at 1.5 m range; mean of 100 measurements with bars indicating ± 1 SD. The *dashed lines* are model predictions. **(a)** 1 m wide plane $(\tau/A = 0.15\,\mu s)$. **(b)** 8.9 cm diam pole $(\tau/A = 0.67\,\mu s)$. **(c)** 8 mm diam rod $(\tau/A = 2.68\,\mu s)$ ▶

simplify the analysis, the peak of the beam profile is approximated with a Gaussian function, a parabola in logarithmic units in Fig. 21.11, to determine the echo amplitude as a function of object bearing θ, or

$$A_\theta = A_0 \exp\left(-\frac{\theta^2}{2\sigma^2}\right), \qquad (21.12)$$
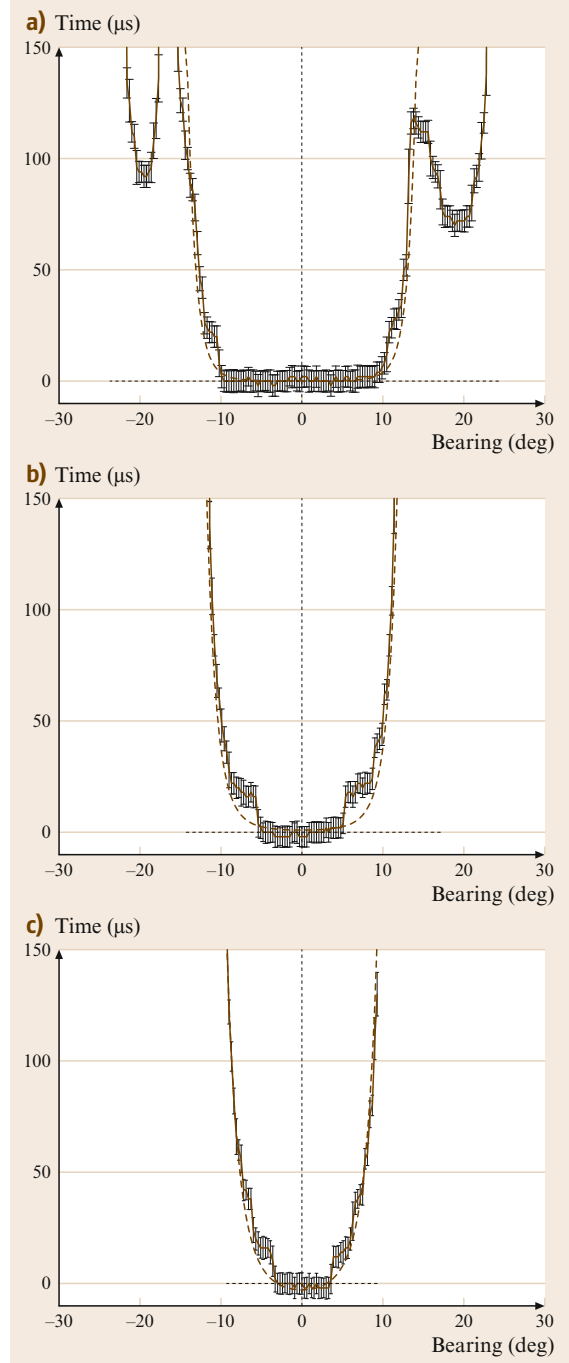
where A_0 is the on-axis amplitude and σ is a measure of the beam width. The value $\sigma = 5.25°$ provides a good fit around the peak of the beam pattern. The

Gaussian model is reasonable only over the central section of the main lobe that produces detectable echoes.

We assume that the echo arrival time t_0 does not change significantly with transducer orientation (object bearing); this effect was investigated and found to be minor [21.4]. In contrast, measured TOFs, denoted by t_m and t'_m in Fig. 21.12, are amplitude dependent and a function of object bearing, which affects echo amplitude as shown in Fig. 21.11.

The module processes the detected echo waveform by rectification and lossy integration, as discussed above. To derive a useful analytic model, assume that the integration is lossless and the rectified echo is a unit step function with amplitude A. This approximates the processed waveform shown in Fig. 21.10b by a linear function around time t_m, shown in Fig. 21.12. The model ignores the residual ripple and the decreasing slope of the waveform as the lossy rectification approaches a constant value, shown in Fig. 21.10. The linear function with a slope proportional to the echo amplitude is given by $A_\theta(t - t_0)$, for $t \geq t_0$. This function exceeds the threshold τ at

$$t_m = t_0 + \frac{\tau}{A_\theta} = t_0 + \frac{\tau}{A_0} \exp\left(\frac{\theta^2}{2\sigma^2}\right) . \qquad (21.13)$$

For fixed τ, the incremental delay in t_m is a function of the bearing θ and inversely proportional to the echo amplitude. When a constant echo amplitude A (in volts) is applied to the integrator, the slope of the linear output is A V/s, with typical values on the order of $A_\theta = 10^5$ V/s. If $\tau = 0.10$ V, $\tau/A_\theta = 10^{-6}$ s $= 1$ μs.

Experiments were conducted with a Polaroid 600 series transducer connected to a model 6500 ranging module [21.38]. The Polaroid module was operated conventionally to generate t_m values as a rotational scan was performed. Objects include a 1 m-wide plane, a 8.9 cm-diameter pole, and an 8 mm-diameter rod, all located at 1.5 m range. A rotational scan was performed from $-40°$ to $+40°$ in 0.3° steps. At each angle, 100 t_m values were recorded. The mean deviations from the t_m when the object is on the sonar axis ($\theta = 0$) were determined

and the standard deviation (SD) values were computed. There were no other objects in proximity to the object being scanned. Echoes from objects beyond 2 m were eliminated by a range gate.

Figure 21.13a shows the data for the plane, Fig. 21.13b for the pole, and Fig. 21.13c for the rod. The values are shown relative to the t_m value observed at 0° bearing. Dashed lines indicate the values predicted by the model. The t_m values showed a variation with SD $= 5$ μs (0.9 mm) at zero bearing, which is about nine times greater than that predicted by sampling jitter alone. This random time jitter is caused by dynamic thermal inhomogeneities in the air transmission medium, which change the local sound speed and cause refraction [21.36, 39]. The SD increases with deviation from zero bearing because smaller echoes exceed the threshold later in the processed waveform. The smaller slope of the latter part of the processed echo waveform shown in Fig. 21.10 causes greater t_m differences for a given variation in echo amplitude, thus increasing the SD.

One feature in the data not described by the model is due to residual ripple in the integrator output, which causes jumps in TOF readings equal to half periods (10 μs) added to the value predicted by (21.13). These jumps are clearly evident in the mean values of Fig. 21.13.

The angular extent over which echoes were detected was 45° for the plane, 22.8° for the pole, and 18.6° for the rod. Side-lobes produced by the plane are visible and have small echo amplitudes, which cause their t_m values to be retarded in time. These angular extents can be related to the echo amplitudes that would have produced the respective arcs according to the piston model; these are indicated in Fig. 21.11. For the plane, the threshold level relative to the maximum echo amplitude is -38 dB, for the pole -25 dB, and for the rod -13 dB. Since the ranging module threshold at 1.5 m range is the same for each object, the difference in levels indicates the relative echo strength from each object, i.e., the plane echo is 13 dB (a factor of 4.5) greater than the pole echo, and the pole echo is 12 dB (a factor of 4) greater than the rod echo.

21.9 Echo Waveform Coding

Systems that display echo information beyond the first echo have been investigated [21.11, 17, 24, 40–42], but typically employ custom electronics. One motivation for examining the entire echo waveform is the success of

diagnostic medical ultrasound imaging systems, which adopt this method [21.43, 44].

As a less expensive alternative to analog-to-digital conversion, the Polaroid ranging module can detect
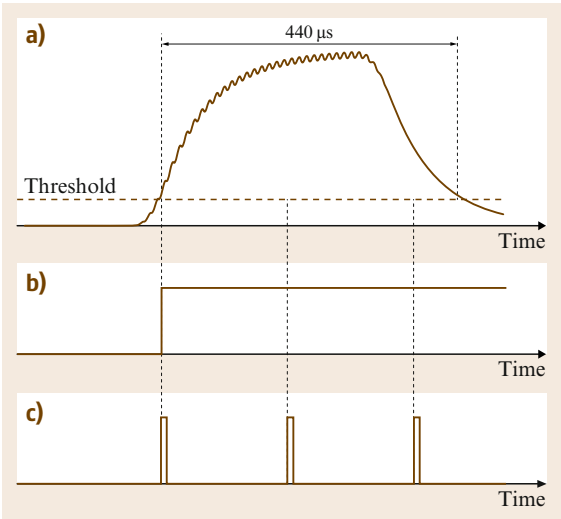
Fig. 21.14a–c Polaroid ranging module operation modes. **(a)** Processed echo waveform. **(b)** *ECHO* output produced in conventional time-of-flight mode. **(c)** *ECHO* output produced in PAS mode

Object		Arc extent (deg)
Plane		48.3
8.9 cm dia post		24.6
2.85 cm dia post		23.1
8 mm dia pole		21.9
1.5 mm dia wire		19.2
0.6 mm dia wire		10.5

Fig. 21.15 PAS sonar maps of six objects located at 1 m range. The sonar is located below the objects in the figure

echoes beyond the initial echo by repeatedly resetting the detection circuit. The 6500 module specification suggests a delay before resetting to prevent the current echo from retriggering the detection circuit [21.3]. Let us ignore this suggestion and control the Polaroid module in nonstandard way to provide information about the entire echo waveform. Since the echo amplitude is estimated from the digital output produced by the Polaroid module, this operation has been called *pseudo-amplitude scan* (PAS) sonar [21.23].

The conventional ranging module processes detected echoes by performing rectification and forming a lossy integration, as illustrated in Fig. 21.14a.

The *BLNK* input is typically kept at zero logic level, which enables the *ECHO* output. *ECHO* exhibits a transition at the time when the processed echo signal exceeds a threshold, as shown in Fig. 21.14b. By convention, the time interval between the *INIT* and *ECHO* transitions indicates the time of flight (TOF), from which the range *r* of the reflecting object is calculated by

$$r = \frac{c \times \text{TOF}}{2} \,. \tag{21.14}$$

Echoes occurring after the initial echo can be detected by resetting *ECHO* by pulsing the *BLNK* input. The specification suggests that the *BLNK* pulse should be delayed after the *ECHO* indication by at least 440 μs to account for all 16 returning cycles in the echo and to
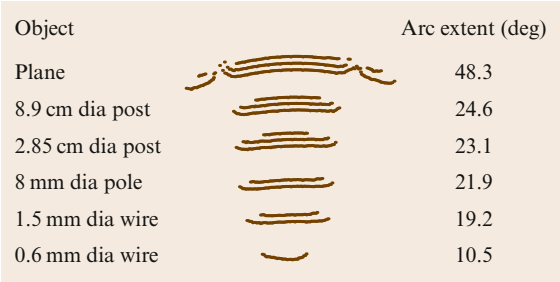
allow it to decay below the threshold for the largest observable echo. The largest echoes typically saturate the detection circuit, providing a predetermined maximum value. This duration corresponds to the time interval over which the processed signal is above the threshold, as shown in Fig. 21.14a.

When an *ECHO* event is observed, the PAS system issues a short 3 μs (corresponding to a software query period) pulse on the *BLNK* input line, which clears the *ECHO* signal as shown in Fig. 21.14c. Upon being cleared, the Polaroid module exhibits a delay inversely related to the echo amplitude, lasting at least 140 μs for large-amplitude echoes, and then produces another *ECHO* event if the processed echo signal still exceeds the threshold. The PAS system repeatedly issues a *BLNK* pulse whenever an *ECHO* event is observed. Hence, a strong echo is represented by three pulses on the *ECHO* line, the first corresponding to the conventional TOF, followed by two more pulses. Because lower amplitude echoes spend less time above the threshold, a weaker echo produces two pulses spaced farther apart, and a very weak echo may produce only one pulse.

A PAS sonar map is generated by placing a range dot along the transducer axis as a rotational scan is executed. With multiple readings per interrogation pulse, a PAS sonar map contains multiple dots at each interrogation angle. Rotational scans then form arcs, with isolated arcs indicating weak echoes, arc pairs moderate echoes, and arc triplets large echoes. To illustrate, Fig. 21.15 shows arcs formed by a large plane (2.3 m width by 0.6 m height) and five cylinders with different diameters, all placed at 1 m range. Examining objects at the same range eliminates effects caused by the range-dependent gain of the module.

A conventional TOF sonar map by comparison would display only the nearest arc in the PAS map for each object. Qualitatively, the arc length increases and the number of arcs increase with the echo amplitude,
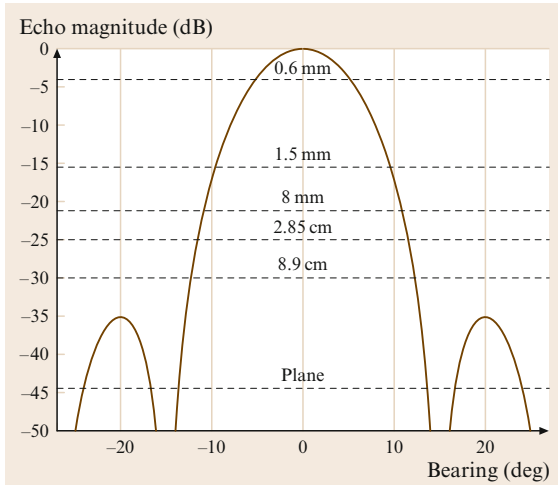
Fig. 21.16 Transmitter–receiver beam pattern. *Dashed lines* indicate the equivalent threshold level for each object

Fig. 21.17 PAS sonar map of 2.85 cm-diameter post (p) and 8.9 cm-diameter post (P). The transducer is located at (0,0). A: Artifact caused by echo originating at transmitter T, reflected by p, bouncing off P back to p, and directed toward receiver R. ($T \rightarrow p \rightarrow P \rightarrow p \rightarrow R$). B: $T \rightarrow P \rightarrow p \rightarrow P \rightarrow$ R. C: $T \rightarrow p \rightarrow P \rightarrow R$ and $T \rightarrow P \rightarrow p \rightarrow R$

which is bearing dependent. The strongest reflectors produce concave arcs [21.4, 45]. This occurs because, with echo amplitudes much greater than the threshold, the threshold is exceeded near the beginning of the echo, yielding a nearly constant range reading over a significant extent over bearing. In contrast, the weakest reflectors produce convex arcs, caused by echoes whose amplitudes are comparable to the threshold. As the echo amplitude decreases the threshold is exceeded at later points along the processed waveform, producing greater range readings. This effect also appears at the edges of the arcs produced by strong reflectors.

Computing the beam pattern of the vibrating piston model [21.1], which is a reasonable approximation to the Polaroid transducer, yields the curve shown in Fig. 21.16. This figure describes the detected echo magnitude normalized to have a maximum of 0 dB, which occurs along the beam axis. The larger echoes are much greater than the threshold, such as those produced by the plane, whose maximum amplitudes can be 44 dB relative to the threshold. The -44 dB threshold agrees with the PAS map for a plane: strong echoes (three stripes) occur within 10° of normal incidence, range readings increase due to echo amplitude reduction at ±15.6°, approximating the predicted nulls at ±14.7°, and smaller-amplitude echoes from the side-lobes are present. Weaker reflectors correspond to larger thresholds when their on-axis echoes normalize to 0 dB. The beam pattern model explains how arc length varies with object reflecting strength. The indicated thresholds were found by matching the angular beam width to the arc extent.
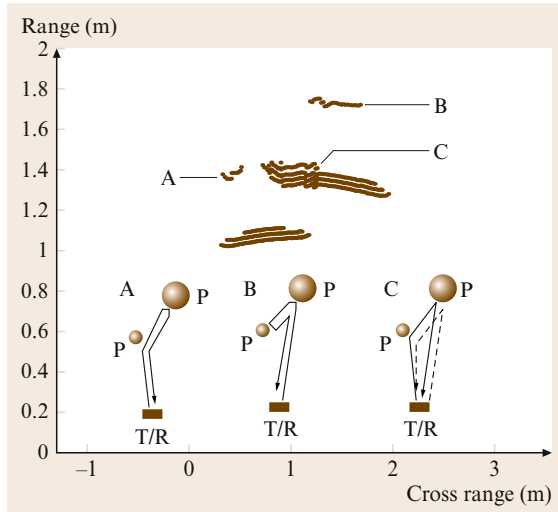
It is apparent that PAS maps provide information useful for solving the inverse problem, that of determining the identity of the object from the echoes. Figure 21.15 shows that PAS maps contain information about the echo amplitude. While it is true that the conventional TOF sonar maps, represented by the closest arc, can determine the object location from the arc center and can infer the echo amplitude from the arc extent, it is also true that this information is presented in a more robust way in the PAS maps. For this simple case of isolated objects, the posts can be clearly differentiated from the pole, while the corresponding conventional TOF arcs are comparable. A tenfold increase in post diameter yields only a modest increase in the conventional TOF arc length, while increasing the number of arcs from two to three in the PAS maps.

When examining the entire echo waveform, one must account for artifacts that are produced when objects interact acoustically. Some artifacts occur after the first detected echo, so these are not a problem in TOF sonar maps [21.4], but must be addressed in interpreting PAS maps. Consider a simple environment consisting of two posts: a 2.85 cm-diameter post (p), located at $r = 1$ m and bearing 12°, and an 8.9 cm-diameter post (P), at $r = 1.3$ m and bearing $-10°$. The corresponding

PAS map shown in Fig. 21.17 displays the echoes from the two objects plus additional echoes that illustrate two types of multiple reflection artifacts. The first type, indicated by A and B, results when only one object is within the transducer beam. An interrogation pulse that is redirected by a reflected object must be directed back to the receiver within its beam pattern in order to be detected. The paths that do this are shown in the figure. The single-arc convex shape of A indicates that the echo has a small amplitude. This is reasonable since both reflectors are nonplanar, and hence weak.

The second type of artifact (C) shown in Fig. 21.17 occurs when both objects are within the beam pattern.

This allows two distinct paths for the echoes to return to the receiver, occurring in opposite directions and doubling the artifact amplitude. With both objects lying near the beam edges, the echo amplitude is small. Since the distance traveled by these echoes is slightly greater than the range to the farther object, this artifact shows a range slightly beyond the more distant object. The superposition of these two components makes the echo from the farther object appear spread out in time. This pulse stretching explains why four arcs are observed, and at one angle five arcs. If the bearing angle between p and P was increased to exceed the beam width, this artifact would disappear.

21.10 Echo Waveform Processing

In this section pulse-echo sonar that processes sampled digitized receiver waveforms is described. These systems offer superior performance over the simple Polaroid ranging module systems described above, which report the TOF based on a threshold. Echo waveform processing does however incur the overhead of more-complex electronics and signal processing and is not readily available commercially.

21.10.1 Ranging and Wide–Bandwidth Pulses

It is shown in [21.11, 46] that the maximum-likelihood estimator (MLE) for the TOF is obtained by maximizing the correlation $\mathrm{cor}(\tau)$ between the received pulse $p(t)$ (containing Gaussian white noise) and the known pulse shape shifted by τ, $\mathrm{rec}(t - \tau)$

$$\mathrm{cor}(\tau) = \frac{\int_a^b p(t)\mathrm{rec}(t - \tau)\,\mathrm{d}t}{\sqrt{\int_a^b p^2(t)\,\mathrm{d}t \int_a^b \mathrm{rec}^2(t)\,\mathrm{d}t}}\,, \qquad (21.15)$$

where the pulse extends from time a to b. The known pulse shape at the receiver depends on the angle of transmission and reception with respect to the normals of the respective transducers. The pulse shape can be obtained by collecting a good signal to noise pulse at 1 m range at normal incidence to the receiver and transmitter and using elliptical impulse response models to obtain template pulses at angles different to normal incidence. Pulse shape also changes with range due to the dispersive properties of absorption due losses in air transmission. These can be modeled using an estimate of the impulse

response due to one meter path through air as is done in [21.11].

The correlation, $\mathrm{cor}(\tau)$ is normalized in (21.15) to be between -1 and $+1$. The correlation at the maximum thus gives a good indication of the match between the expected and actual pulse shapes and can be used to assess the quality of the TOF estimate. In practice (21.15) is used in discrete time form, where the integrals are replaced by sums of products and digital signal processors are an ideal implementation since they are highly optimized to perform this calculation [21.47, 48]. To achieve an arrival time estimator with resolution smaller than the discrete time sample rate, parabolic interpolation can be used on the maximum three correlations [21.11]. Of interest is the jitter standard deviation σ_R in the TOF estimator due to receiver noise. From [21.11, 46]

$$\sigma_R = \frac{\sigma_n}{B\sqrt{\sum_k \mathrm{rec}(kT_s)^2}}\,, \qquad (21.16)$$

where the summation index k is over the entire receiver pulse sampled every T_s seconds (1 μs in [21.11, 47]), B is the bandwidth of the receiver pulse, and σ_n is the standard deviation of the receiver noise. Equation (21.16) shows that broadband high-energy pulses achieve low errors in the TOF estimator. In [21.11] this is achieved by using a 300 V pulse to excite the transmitter and achieve close to the impulse response from the device with a pulse shape similar to that shown in Fig. 21.6d.

21.10.2 Bearing Estimation

There are many proposed methods for bearing estimation. A single transducer [21.49] can be used by

exploiting the dependency of the received pulse shape on the angle of reception. This approach works for angles within one half of the beam width since the pulse shape is symmetric with respect to the transducer normal angle. Differences in zero-crossing times either side of the maximum amplitude of the pulse are used to obtain an accuracy of the order of 1°. Other single-receiver techniques rely on repeated measurements from a scan across the scene [21.50, 51] and achieve a similar level of accuracy but at much slower sensing speed since multiple readings are necessary.

Other single measurement approaches rely on two or more receivers [21.11, 12, 24]. This gives rise to a correspondence problem where data must be associated between the receivers. The closer the spacing between receivers, the simpler and more reliable the correspondence procedure. The misconception that bearing accuracy improves with larger receiver spacing ignores the correlation between measurement errors that can arise due to the measurements sharing an overlapping space of air in the propagation of the ultrasound. Due to the high accuracy of TOF estimation in [21.11] the receivers could be spaced as close as physically feasible (35 mm) and still bearing accuracies lower than any other systems are reported. Standard deviations of bearing errors are reported to be below 0.2° for a plane at a range of 4 m within a −10° to +10° beam width.

There are two common approaches to bearing estimation – interaural amplitude difference (IAD) [21.52] and interaural time difference (ITD) [21.11, 24, 47–49, 52]. IAD uses two receivers pointing away from each other so that an echo has a different amplitude response in each receiver's beam width. In ITD both receivers usually point in the same direction and the TOF is measured on each receiver and triangulation is applied to determine the angle of arrival. The bearing calculation is dependent on the target type, such as a plane, corner or edge; these geometries are analyzed in [21.11]. A simple arrangement with a transceiver and receiver is shown in Fig. 21.18, where T/R1 is the transceiver and R2 is the second receiver, spaced a distance d from each other. The virtual image of the transmitter is shown as T′. The two TOFs measured on the two receivers are t_1 and t_2, and these are used to estimate the bearing angle, θ, to the plane which is the angle to the plane normal. Applying the cosine rule to the triangle R2 R1 T′ in Fig. 21.18 gives

$$\cos(90 - \theta) = \sin \theta = \frac{d^2 + c^2 t_1^2 - c^2 t_2^2}{2dct_1} . \quad (21.17)$$
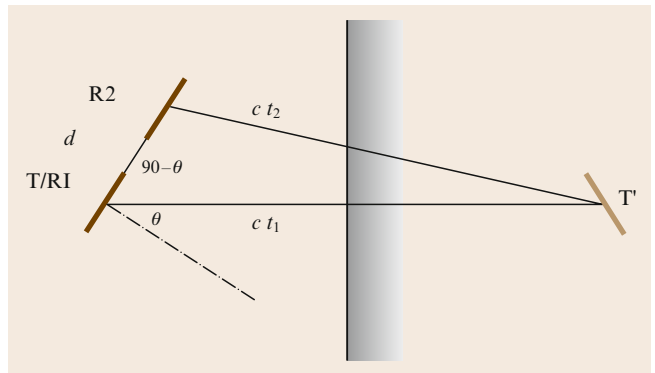
Fig. 21.18 Bearing (θ) calculation for a plane using a transceiver T/R1 and a receiver R2. T′ is the virtual image of T

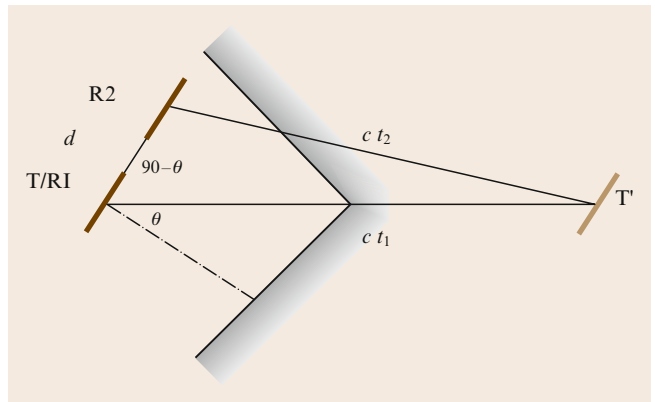**Fig. 21.19** Bearing (θ) calculation for a corner using a transceiver T/R1 and a receiver R2. T′ is the virtual image of T
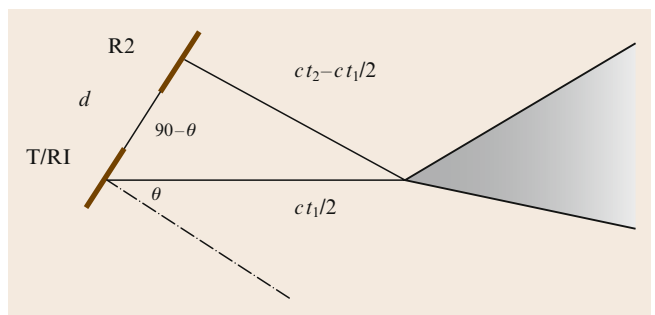

Fig. 21.20 Bearing (θ) calculation for an edge using a transceiver T/R1 and a receiver R2. No virtual image is present since the edge radiates from a point source at the edge

When $d \ll ct_1$, (21.17) can be approximated by

$$\sin \theta \approx \frac{c(t_1 - t_2)}{d} . \quad (21.18)$$

Note that any common (i. e., correlated) noise in t_1 and t_2 is removed by the difference in (21.18) and hence the correlation in noise components of the TOF cannot be overlooked in bearing estimation as described above.

The situation for a corner is shown in Fig. 21.19 and the same result applies as in (21.17). For an edge the situation is shown in Fig. 21.20, where R1 has a TOF from T to the edge and back to R1, whilst R2 has a TOF from T to the edge and back to R2. From the geometry,

we use the same approach as in (21.17) to give

$$
\begin{aligned}
\sin\theta &= \frac{d^2 + c^2 t_1^2/4 - c^2(t_2 - t_1/2)^2}{2dct_1/2} \\
&= \frac{d^2 + c^2 t_2(t_1 - t_2)}{dct_1} \; .
\end{aligned} \tag{21.19}
$$

Note that (21.19) can be approximated by (21.18) when $d \ll t_1$.

21.11 CTFM Sonar

Continuous-transmission frequency-modulated (CTFM) sonar differs from the more common pulse-echo sonar discussed in previous sections in the transmission coding and the processing required to extract information from the receiver signal.

21.11.1 CTFM Transmission Coding

The CTFM transmitter continuously emits a varying-frequency signal, usually based on a sawtooth pattern as shown in Fig. 21.21, where the frequency is often swept through an octave every sweep cycle T. The transmitted signal with a linearly changing frequency can be expressed as

$$
S(t) = \cos[2\pi(f_{\mathrm{H}}t - bt^2)] \tag{21.20}
$$

for $0 \le t < T$. The sweep cycle is repeated every T seconds as shown in Fig. 21.21. Frequency is $1/2\pi$ times the time derivative of the phase in (21.20). Note that the highest frequency is f_{H} and the lowest transmitted frequency is $f_{\mathrm{H}} - 2bT$, where b is a constant that de-

Fig. 21.21 Plot of frequency versus time for CTFM. The blind time applies if the shown echo corresponds to a maximum range target at R_{m}

termines the sweep rate. We can then define the swept frequency ΔF as

$$
\Delta F = 2bT \; . \tag{21.21}
$$

21.11.2 CTFM TOF Estimation

Echoes are generated when the transmitted wavefront encounters reflectors and are an attenuated, delayed version of the transmitted signal

$$
E(t) = A S\left(t - \frac{2R}{c}\right) , \tag{21.22}
$$

where R is the range to the reflector, c is the speed of sound and A is the amplitude that may in the case of curved objects depend on the frequency of the sound at reflection.

The TOF is estimated by the two step process of demodulation and spectral analysis. Demodulation is achieved by multiplying the received signal by a copy of the transmitted signal and low pass filtering. This can best be understood in the simple case of one echo. The signal $D(t)$ is obtained using (21.20) and (21.22)

$$
\begin{aligned}
D(t) &= E(t)S(t) \\
&= \frac{A}{2}\Big[\cos\left(2\pi f_{\mathrm{e}}t - \phi\right) \\
&\quad + \cos\left(2\pi f_{\mathrm{u}}t - 2bt^2 - \phi\right)\Big] \\
\text{for } f_{\mathrm{e}} &= \frac{4Rb}{c} , \\
f_{\mathrm{u}} &= \left(2f_{\mathrm{H}} + \frac{4Rb}{c}\right) , \\
\phi &= f_{\mathrm{H}}\frac{2R}{c} + \frac{4bR^2}{c^2} ,
\end{aligned} \tag{21.23}
$$

where the following trigonometric identity has been used in (21.23)

$$\cos(x)\cos(y) = \frac{1}{2}[\cos(x-y) + \cos(x+y)] . \tag{21.24}$$

A low-pass filter removes frequency components above f_H and this results in the base-band signal:

$$D_b(t) = \frac{A}{2}\left[\cos\left(2\pi\frac{4Rb}{c}t - \phi\right)\right] \tag{21.25}$$

which has a frequency proportional to the range R. The ranges of echoes can be extracted by examining the spectrum of D_b using, for example, a discrete Fourier transform (DFT) or the fast Fourier transform (FFT) if the number of samples is a power of 2. From (21.25) for a frequency peak of f_r Hz the corresponding range R is given by

$$R = f_r\frac{c}{4b} . \tag{21.26}$$

Note that the above analysis relies on excluding the receiver waveform at the start of each sweep for a *blind time* (Fig. 21.21) of $R_m/2c$, where R_m is the maximum target range. During this blind time the receiver signal is dependent on the previous sweep rather than the current sweep as assumed in the analysis above. The sweep time T needs to be much larger than this blind time for the sonar to operate effectively. The blind time can be eliminated at the expense of introducing complexity in the demodulation process as described in [21.53], where an interlaced double demodulation scheme is described.

21.11.3 CTFM Range Discrimination and Resolution

We define range discrimination as the separation in range of two targets that can be simultaneously detected as distinct. The range resolution is defined as the smallest increment in range that can be measured by the sonar.

Suppose that, in order to extract ranges of targets, $D_b(t)$ from (21.25) is sampled at ΔT intervals and k samples are collected before a DFT (or FFT if k is a power of 2) is performed. The frequency samples of the DFT will be $\Delta f = 1/(k\Delta T)$ apart. From (21.26), this represents a range resolution ΔR of

$$\Delta R = \frac{c\Delta f}{4b} = \frac{c}{4bk\Delta T} . \tag{21.27}$$

We can relate this to the swept frequency ΔF from (21.21) as

$$\Delta R = \frac{c}{2\Delta F} \times \frac{T}{k\Delta T} , \tag{21.28}$$

where the second term is the ratio of the sweep time to the spectral sample time. In order to discriminate two peaks in the DFT, they must be at least two samples apart and hence

$$\text{range discrimination} = \frac{c}{\Delta F} \times \frac{T}{k\Delta T} . \tag{21.29}$$

Note that (21.28,21.29) show that, subject to signal-to-noise constraints, CTFM can lengthen the *data integration time* $k\Delta T$ in order to improve the range discrimination and resolution of the sonar. Also it is possible, subject to signal noise, to use interpolation techniques (e.g., parabolic interpolation) on the DFT peaks to resolve to a smaller than Δf frequency and hence improve range resolution (but not range discrimination).

21.11.4 Comparison of CTFM and Pulse–Echo Sonar

- The range resolution of pulse-echo sonar and CTFM sonar is theoretically the same given the same signal-to-noise ratios and bandwidths [21.53]. The range discrimination in pulse-echo sonar is limited by the pulse length, where shorter pulse lengths require higher bandwidth. However in CTFM, range discrimination can be improved by increasing the data integration time, allowing more design flexibility.
- CTFM also allows for the energy of the transmitted signal to be spread evenly over time, resulting in lower peak acoustic power emission compared to pulse-echo systems with the same receiver signal-to-noise ratio. CTFM can provide a greater average power in a practical context and consequently a greater sensitivity to weak reflectors is possible.
- CTFM requires more-complex transmitter circuitry and the requirement for FFT processing on the receiver side.
- Separate transmitter and receiver transducers are necessary with CTFM, whilst pulse-echo systems can use a single transducer for both transmission and reception, resulting in restriction on the minimum range of pulse-echo sonar due to the blanking of the receiver during transmission. CTFM has no inherent restriction on minimum range.
- CTFM sonar can continuously derive range information from targets every $k\Delta T$ seconds at a delay of $R/c + k\Delta T$ compared to every $2R_m/c$ with a delay of $2R/c$ in pulse-echo sonar (ignoring processing

delays in both), which may be important in real-time tracking applications.
- Other benefits of CTFM are that the number of range measurements per cycle is limited only by the range discrimination constraint of (21.28) and the signal-to-noise ratio.
- In terms of bearing estimation and classification of targets from a moving platform, short pulse-echo sonar systems like [21.26, 47] do not suffer from the CTFM data integration time required to estimate accurately the frequencies corresponding to ranges (and hence bearing). During the data integration time, the target can move with respect to the sensor and blur the measurements, making bearing estimation and classification less accurate. In short pulse-echo systems, the target is effectively sampled with a pulse of less than 100 μs, resulting in a consistent snapshot of the target.

21.11.5 Applications of CTFM

Kay [21.54, 55] developed a mobility aid for blind people using a CTFM sonar system based on a sweep of $f_H = 100$ kHz down to 50 kHz with a sweep period of $T = 102.4$ ms. After demodulation, ranges are heard as audible tones with frequencies up to 5 kHz corresponding to ranges of up to 1.75 m. The system uses one transmitter and three receivers as shown in Fig. 21.22. Users of the system can listen to the demodulated signal in stereo headphones corresponding to the left and right receivers, each mixed with the large central oval receiver. Higher frequencies correspond to more-distant ranges. To illustrate the sensitivity, a 1.5 mm-diameter wire is easily detectable at 1 m range – the echo produced is 35 dB above the noise floor in the system.

CTFM sonar has been used to recognize isolated plants [21.40, 56]. The advantage gained from CTFM is that extensive range and echo amplitude information is obtained from the whole plant given the spectrum of the demodulated received signal, and these echoes are obtained from an excitation across an octave of frequencies from 100 down to 50 kHz with a high signal-to-noise ratio that allows weak reflections from leaves to be sensed. This information is called the *acoustic density profile* and 19 different features are found to be useful in classifying the plants, such as the number of range cells above a threshold in amplitude, the sum of all range cells, the variation about the centroid, the distance from the first to the highest amplitude cell, and the range over which reflections are detected. With

Fig. 21.22 Aid for blind people – the small oval transducer is the transmitter and the other three components are receivers. The large oval receiver provides high resolution, enabling fixation by users' fine neck control (Photo courtesy [21.54])

a population of 100 plants, an average of 90.6% correct pairwise classification was obtained using a statistical classifier.

Scanning CTFM with a singe transmitter and single receiver has been successfully applied to mapping of indoor environments that include smooth and rough surfaces [21.51] with bearing errors on the order of 0.5° for smooth surfaces and higher for edges. The classification uses amplitude information that is normalized with range using a fixed attenuation constant of sound. In practice this attenuation constant varies with temperature and humidity and needs to be calibrated before each experiment for consistent results. Greater robustness, speed, and accuracy has been demonstrated with TOF methods of classification that require at least two transmitter positions and two receivers as described in [21.11, 47]. CTFM could be applied to array systems to achieve higher sensitivity to weak targets than the existing pulse-echo systems.

CTFM has been employed in three binaural systems [21.12] where a rigorous theoretical and experimental comparison of these ultrasonic sensing systems based on different range and bearing estimators is made. *Stanley* [21.12] also contains detailed engineer-

ing design information of CTFM sonar systems. The conclusion is that CTFM can insonify large areas due to its higher average power transmissions and consequently good signal to noise performance. The use of autoregressive estimators for spectral lines in the demodulated signal were found to provide better res-

olution than the DFT. The interaural distance and power difference CTFM approaches provided state-of-the-art performance except that the pulse-echo approach in [21.11] using a high-energy short pulse was found to be a *factor of six to eight* times superior in bearing precision.

21.12 Multipulse Sonar

This section examines sonar systems that employ more than one pulse in the transmitter(s). The main motivations are interference rejection and on-the-fly classification. Multipulse sonar has also been used to generate a better signal-to-noise ratio by creating longer transmitted pulse sequence using Barker codes [21.57]. The autocorrelation of a Barker code gives a narrow peak with low autocorrelation away from the central lobe. The matched filter then gives rise to pulse compression that averages noise over a longer time period.

21.12.1 Interference Rejection

External acoustic noise, such as compressed air, is a source of sonar interference. Sonar systems attempt to reduce the effects of external interference by filtering the signal and the optimal filter is the matched filter where the impulse response is the time reversal of the pulse shape that is expected. Since a time-reversed convolution is a correlation, the matched filter then acts as a correlation with the expected pulse shape as discussed in Sect. 21.10. Approximations to matched filtering can be designed based on a bandpass filter with a frequency response that is similar to the spectrum of the expected receiver pulse. CTFM systems allow robust suppression of external interference by employing a matched filter across a broad range of frequencies contained in the continuous chirp transmission.

When more than one sonar system operates in the same environment, the transmitted signal from one sonar system can be received by another, causing crosstalk errors. This is particularly evident in classical sonar rings constructed from Polaroid ranging modules. Error-eliminating rapid ultrasonic firing strategies have been developed [21.58] and are claimed to remove most of this interference and allow faster operation of these sonar rings.

More-sophisticate coding of transmitted pulse(s) has been employed [21.22, 59–62] to allow rejection of external interference and crosstalk. One difficulty with

multiple transmitted pulses over an greater time period than a single pulse is that target clutter can produce many overlapping pulses at the receivers that are difficult to unravel and interpret, and the sonar range discrimination can be compromised.

21.12.2 On-the-Fly Target Classification

Target classification into planes, cylinders, and edges has been achieved by deploying a single transmitter and three receivers [21.24] using a single measurement cycle. At least two transmitters are required to differentiate planes from concave right-angled corners [21.11] where a two transmitter arrangement is used to classify targets into planes, corners, and edges in two successive measurement cycles. The method of classification can be understood with virtual images and mirrors, since specular sonar reflections occur. Looking into a plane mirror gives an image that is left–right reversed compared to looking into a right-angled mirror. An edge is analogous to observing a high-curvature specular surface, such as a polished chair leg, where the whole image is compressed to a point. Sonar classification exploits the difference in bearing angles to a target from two transmitters to classify as follows: a positive difference δ indicates a plane, a negative δ value indicates a corner, and zero difference an edge, where the angle δ depends on the sensor geometry and target range. More sophistication can be added by using range measurements in addition to bearing, with maximum-likelihood estimation.

This arrangement [21.11] was refined to work with just one measurement cycle of around 35 ms to 5 m range: hence the term *on-the-fly* in [21.47]. This on-the-fly approach uses pulses fired at a precise time difference ΔT and 40 mm apart from two transmitters with two further receivers completing a square. ΔT is usually around 200 μs but can vary randomly from cycle to cycle to achieve interference rejection (both crosstalk and environmental) with identical sonar systems. Classification is performed simultaneously in one measurement cycle.

The sensor achieves high accuracy in range and bearing with robust classification by exploiting the tight correlation between TOF jitter in the different transmitter to receiver paths due to the close temporal and spatial arrangement. The sensor has been deployed for large-scale mapping in [21.63].

21.13 Sonar Rings

21.13.1 Simple Ranging Module Rings

Since sonar only detects objects lying within its beam, a common means to scan the entire environment outside the robot is to use an array of sonars, or a *ring* [21.64]. The most common is the Denning ring that contains 24 sonars equally spaced around the robot periphery. This 15° spacing allows some overlap in the sonar beams so at least one of the sonars will detect a strong reflecting object. The sonars in the ring are typically employed sequentially one at a time. Using a 50 ms probing pulse period to reduce false readings a complete environmental scan is accomplished every 1.2 s. This sample time is adequate for a translate-and-stop operation in research settings, but may be too slow for a continually moving robot. A robot moving at 1 m/s may not detect an object with sufficient warning to prevent a collision. Some researchers propose simultaneously employing sonars on opposite ends of the
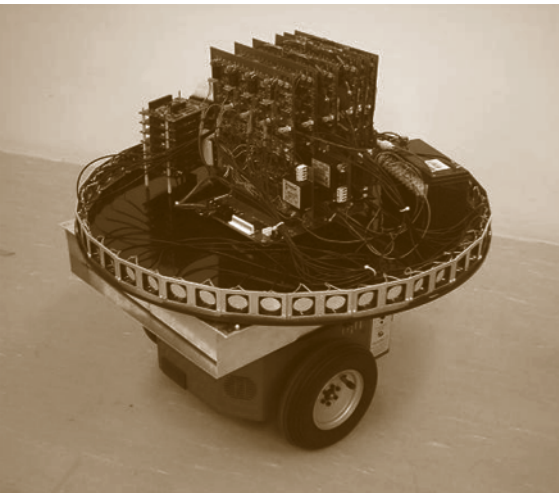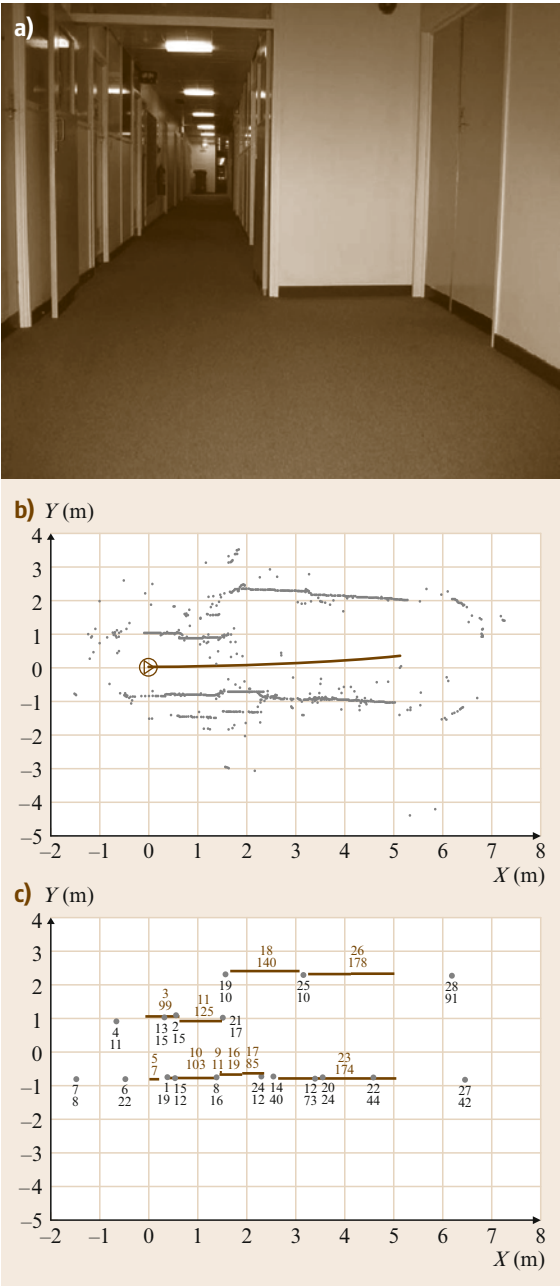

Fig. 21.23 DSP sonar ring hardware

Fig. 21.24a–c DSP sonar ring mapping an indoor environment (**a**), raw data (**b**) and SLAM feature map with feature number and number of associations shown as numbers (**c**). The sonar ring is moving at 10 cm/s with a 11.5 Hz sampling rate ▶

ring to speed up acquisition times, while others also reduce the probing pulse period and attempt to identify artifacts.

21.13.2 Advanced Rings

Yata et al. [21.49] developed a 32 cm-diameter sonar ring with 30 transmitters and 30 receivers placed alternately. Murata piezoelectric MA40S4R wide-angle transducers are used to enable overlapping reception of echoes produced by firing all the transmitters simultaneously. An axial symmetrical exponential horn structure is used to narrow the beam shape of the transmitters vertically to avoid reflections from the floor. Received signals are compared with a decaying threshold to produce a 1 bit digitized sampled signal without rectification. Bearing is estimated from the leading edge of echoes and an error standard deviation of 0.4° is reported for ranges up to 1.5 m.

A sonar ring with seven digital signal processors (DSPs) [21.48, 65, 66] that uses 24 pairs of 7000 series Polaroid transducers consisting of a transceiver and receiver has been developed (Fig. 21.23). Each pair can derive range and accurate bearing information using template-matching digital signal processing (Sect. 21.10) on each of the two receiver channels, which are sampled at 250 kHz with 12 bit analog to digital converters. In total eight receiver channels are processed per DSP. All transceivers are fired simultaneous to enable full surrounding sensing of the environment approximately 11 times a second to a 6 m range with experimentally validated range and bearing accuracies to smooth targets of 0.6 mm and 0.2°, respectively. To suppress interference between neighboring pairs, two different transmitted pulse shapes are employed in an interleaved fashion around the perimeter of the ring. The pulse shapes are derived from two and three cycles of 65 kHz excitation. The DSP sonar ring allows rapid and accurate wall following, map building, and obstacle avoidance due to the high repetition and accurate range and bearing sensing. The beam width of the transducer pairs allows full 360° coverage with respect to smooth specular targets to a range of 3 m. An example of the DSP sonar ring producing a feature for a simultaneous localization and mapping (SLAM) map is shown in Fig. 21.24.

21.14 Motion Effects

When a sensor moves with respect to its targets, sonar measurements are effected. For example, a sonar sensor moving at a speed of 1% of the speed of sound (around 3.4 m/s) will experience errors of the order of 0.6° for some bearing measurements. The effects of linear velocity on the TOF and reception angle are dependent on the target type and hence for motion compensation to be meaningful a target classification sensor is needed. We consider the classical plane, edge, and corner target types in this section. Rotational motion effects are discussed in [21.26] where it is shown that very high speeds of rotation are necessary to give rise to a small bearing error (e.g., 0.1° error for approximately 1700 deg/s). Narrowing of the effective beam width is another effect of high rotation speeds of a sonar sensor.

The sensor is assumed to transmit from a point labeled T and receiver measurements are referenced to this position on the sensor. However, due to the motion of the sensor, the ground referenced position R at the time of reception of the echo moves from T over the course of the TOF. For a linear velocity, the distance between T and R is TOF $\times v$, where v is the magnitude of the sensor velocity vector relative to the ground, with components v_x and v_y parallel to their respective coordinate axes. The expressions derived for linear motion apply to any sonar sensor, since only the physics of sound propagation and reflection are used. All targets are assumed to be stationary.

This section is based on [21.26], where further experimental work not included here can be found.

21.14.1 Moving Observation of a Plane

A plane target reflects the transmission from position T to R as shown in Fig. 21.25a. The TOF is broken up into two parts: t_1 is the time of propagation to the plane and t_2 from the plane to the receiver R. Here we derive the effect of linear motion on the TOF $= t_1 + t_2$ and the angle of reception θ all taken from the view of a *stationary observer*. A moving observer is discussed below.

From the right-angle triangle on the left of Fig. 21.25a, we have

$$\sin \theta = \frac{v_x}{c} \text{ and } \cos \theta = \sqrt{1 - \left(\frac{v_x}{c}\right)^2} \qquad (21.30)$$
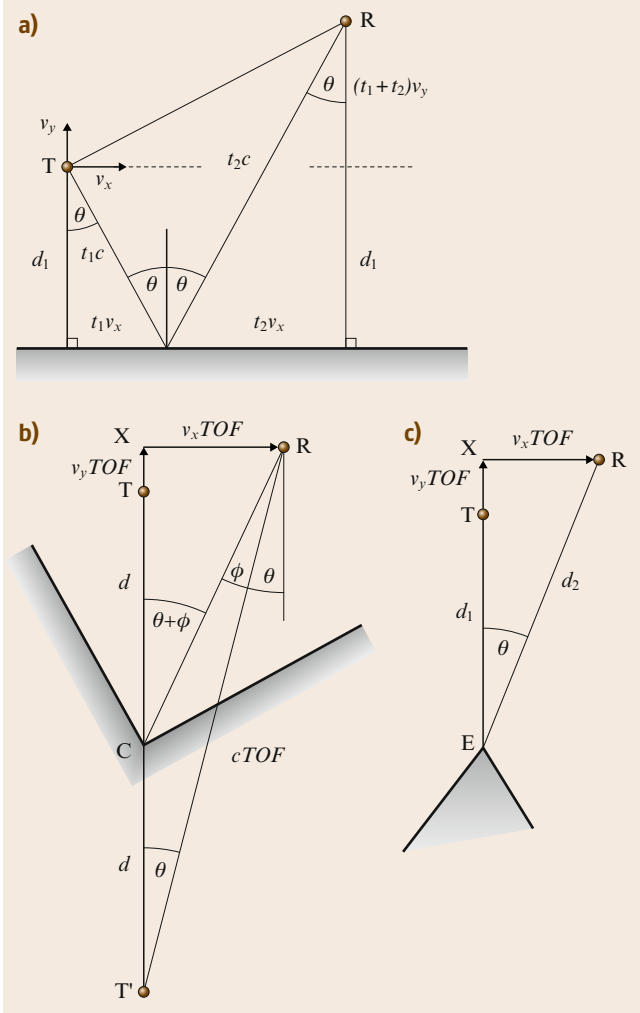
Fig. 21.25a–c Observing a target from a moving sensor. T is the position of the transmitter and R is where the echo is received at the end of the TOF. The target is a plane in **(a)**, a corner in **(b)**, and an edge in **(c)**

and also

$$\cos\theta = \frac{d_1}{t_1 c} \implies t_1 = \frac{d_1}{c\cos\theta} . \tag{21.31}$$

From the right-angled triangle on the right of Fig. 21.25a, we have

$$\cos\theta = \frac{(t_1+t_2)v_y + d_1}{t_2 c} \implies t_2 = \frac{(t_1+t_2)v_y + d_1}{c\cos\theta} . \tag{21.32}$$

The TOF is obtained by adding (21.31) and (21.32) and then substituting (21.31) giving

$$\text{TOF} = \left(\frac{2d_1}{c}\right) \frac{1}{\sqrt{1 - \frac{v_x}{c}^2 - \frac{v_y}{c}}} . \tag{21.33}$$

The first factor in (21.33) represents the stationary TOF. The second factor approaches unity as the velocity approaches zero.

21.14.2 Moving Observation of a Corner

Figure 21.25b shows the situation for a corner with the virtual image of T is shown as T′. From the right-angled triangle T′XR

$$c^2\text{TOF}^2 = (2d_1 + v_y\text{TOF})^2 + v_x^2\text{TOF}^2 \tag{21.34}$$

which gives

$$\text{TOF} = \frac{2d_1}{c}\left[\frac{\sqrt{1 - \left(\frac{v_x}{c}\right)^2} + \frac{v_y}{c}}{1 - \left(\frac{v}{c}\right)^2}\right] , \tag{21.35}$$

where $v^2 = v_x^2 + v_y^2$. The left-hand term of (21.35) is the stationary TOF and the right-hand term approaches unity for small velocities. The angle ϕ in Fig. 21.25b is the angle deviation due to motion as reference by a stationary observer. From the triangles T′XR and CXR

$$\tan\theta = \frac{v_x\text{TOF}}{2d_1 + v_y\text{TOF}} \quad \text{and}$$

$$\tan(\theta + \phi) = \frac{v_x\text{TOF}}{d_1 + v_y\text{TOF}} . \tag{21.36}$$

From (21.36), we have

$$\tan(\theta + \phi) = \left(2 - \frac{v_y\text{TOF}}{d_1 + v_y\text{TOF}}\right)\tan\theta \tag{21.37}$$

and solving for $\tan\phi$ yields

$$\tan\phi = \tan\theta\left(\frac{1 - \sin^2\theta}{\frac{v_y\text{TOF}}{d_1} + 1 + \sin^2\theta}\right)$$

$$= \left(\frac{v_x}{\frac{2d_1}{\text{TOF}} + v_y}\right)\left(\frac{1 - \sin^2\theta}{\frac{v_y\text{TOF}}{d_1} + 1 + \sin^2\theta}\right) . \tag{21.38}$$

For $v_x, v_y \ll c$, $\sin\theta \ll 1$ and $2d_1/\text{TOF} \approx c$ we can approximate (21.38) as

$$\phi \approx \frac{v_x}{c} . \tag{21.39}$$

21.14.3 Moving Observation of a Edge

Since an edge reradiates the incoming ultrasound from an effective point source, the reception angle with respect to a stationary observer is unaffected by motion as shown in Fig. 21.25c. The TOF is affected due to the motion moving the receiving position. From the right-angled triangle XER, $d_2^2 = (d_1 + v_y)^2 + v_x^2 \text{TOF}^2$ and $d_1 + d_2 = c\text{TOF}$ leads to

$$\text{TOF} = \frac{2d_1}{c}\left(\frac{1 + \frac{v_y}{c}}{1 - \frac{v^2}{c^2}}\right) \approx \frac{2d_1}{c}\left(1 + \frac{v_y}{c}\right), \quad (21.40)$$

where the approximate holds in (21.40) for $v \ll c$.

21.14.4 The Effect of a Moving Observation on the Angle of Reception

The expressions for the reception angle in the previous sections are based on an observer that is stationary with respect to the propagating medium air. In practice the observer is the sensor, and is moving with a velocity v. Suppose that the sonar wave arrives at an angle α relative to the air, as shown in Fig. 21.26. The velocity components of the wavefront relative to the observer, w_x and w_y, are as follows

$$w_x = c\sin\alpha - v_x \text{ and } w_y = c\cos\alpha - v_y. \quad (21.41)$$

From (21.41) the observed angle of arrival, β is

$$\tan\beta = \frac{c\sin\alpha - v_x}{c\cos\alpha - v_y} = \frac{\sin\alpha - \frac{v_x}{c}}{\cos\alpha - \frac{v_y}{c}}. \quad (21.42)$$

21.14.5 Plane, Corner, and Edge Moving Observation Arrival Angles

In this section the arrival angles (in radians) for each target type are summarized and approximated for speeds expected of a mobile robot. The speed is assumed
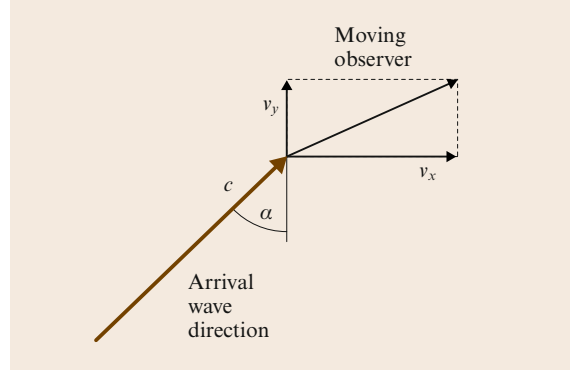

Fig. 21.26 Observation of arriving wave from a moving observer

to be less than a few percent of the speed of sound (typically 340 m/s at room temperature). These effects have been observed experimentally at speeds of up to 1 m/s [21.26].

Equations (21.41) and (21.30) cancel exactly, and for a plane the arrival angle relative to the sensor is exactly zero

$$\beta_{\text{plane}} = 0. \quad (21.43)$$

This can be explained by noting that the forward wave velocity component is always the same as the sensor's as reflection preserves this component.

For a corner the angle ϕ results in a wavefront that appears to be displaced in the same direction as the sensor motion from the real corner direction, as can be seen in Fig. 21.25b. The effect of the moving observer doubles this effect as seen by (21.41) and (21.39)

$$\beta_{\text{corner}} \approx -\frac{2v_x}{c}. \quad (21.44)$$

For an edge the result is due to the observer only

$$\beta_{\text{edge}} \approx \tan^{-1}\left(\frac{0 - \frac{v_x}{c}}{\cos\alpha - \frac{v_y}{c}}\right) \approx -\frac{v_x}{c}. \quad (21.45)$$

21.15 Biomimetic Sonars

The success of biosonars, bats and dolphins [21.67], has led researchers to implement sonars based on biosonar morphology, strategy, and nonlinear processing. The capabilities exhibited by biosonars have caused researchers to examine biomimicking (*biomimetic*) systems.

Biosonar morphology typically has a single transmitter and a pair of receivers. Bats transmit sound pulses through the mouth or nose, while dolphins transmit through a melon. The two receivers correspond to ears that permit binaural processing. Mimicking binaural hearing has led to small arrays that localize objects [21.8]

Fig. 21.27 Biomimetic configuration sonar with center transmitter flanked by receivers that rotate

Fig. 21.28 Biomimetic sonar mounted on the end of a robot arm

and scanning strategies [21.68]. Movable pinnae observed in bats have motivated research in receivers that rotate [21.69, 70]. Figure 21.27 shows one such example.

Rotating the receivers so their axes fall onto the reflecting object not only increases the detected echo amplitude, but also its bandwidth, both effects improving the ability to classify an object.

Biosonar strategy provides clues for successful object localization. It is well known that the object location within the transducer beam affects the echo waveform and complicates the inverse problem of object classification [21.10, 71]. Dolphin movies show that they maneuver to position an object at a repeatable location and range, guided by binaural echo processing. This has motivated a dolphin-mimicking movable sonar positioned at the end of a robot arm for object classification [21.10, 71], as shown in Fig. 21.28. This system was able to differentiate reliably the head and tail side of a coin, but only after introducing a scan in elevation to accommodate for the lack of such positioning afforded by binaural hearing. The idea for a scan over elevation was motivated by the nodding motion that dolphins exhibit when searching for prey lying under the sand.

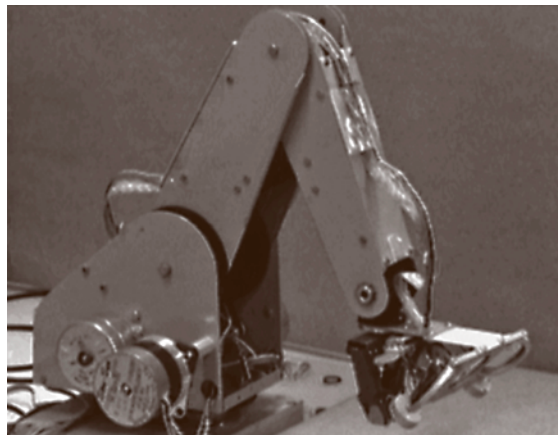Another useful strategy, suggested by probing pulses emitted by bats, is processing echo sequences. As an extension to the conventional stop-and-scan operation of most sonars, sonar data were acquired while the sonar was moving along piecewise linear paths to reveal hyperbolic trends, similar to acoustic flow [21.72]. Matching data to hyperbolic trends permits the estimation of the passing range, which is useful for collision avoidance and passing through narrow openings [21.72].

Most sonar systems use classical estimation procedures involving correlation detection and spectrum analysis. The cochlear model has led to multiple band-pass filters to process wide-band pulses for environmental landmark classification [21.73]. The action potential spikes observed in the biological nervous system also suggest neuromorphic processing based on coincidence detection. The sparse information provided by conventional TOF measurements motivated sonar detectors that provided complete echo waveform information from multiple detections that result in spike-like data [21.23, 74]. Applying temporal and spacial coincidence to spike data has led to reverberation artifact recognition [21.35] and passing-range estimation [21.75].

Such biomimetic techniques provide insights into the information content present in echoes and the type of sensing tasks for which sonar is best suited.

21.16 Conclusions

Sonar is a useful, inexpensive, low-power, light-weight and simple ranging sensor for robotics applications

that can provide accurate object localisation. For sonar to be effectively employed, understanding its physical

principles and implementation is important and these topics are covered in the early sections of this chapter. Various approaches to sonar sensing are highlighted from simple single-transducer ranging to more sophisticated multi-transducer and multi-pulse configurations with associated signal processing requirements. Sophisticated sonars are capable of measuring target range and angle accurately as well as classifying targets, rejecting interference, and compensating for motion. Sonar rings provide surrounding environmental coverage, and CTFM systems improve the sensitivity for detecting small reflectors. Research is ongoing in areas such as signal and data processing, sonar map building, sonar configurations, transducer technology and biomimetic sonar that draw inspiration from biological sonar systems, such as used by bats and dolphins.

References

21.1   L.E. Kinsler, A.R. Frey, A.B. Coppens, J.V. Sanders: *Fundamentals of Acoustics* (Wiley, New York 1982)

21.2   R.C. Weast, M.J. Astle (Eds.): *CRC Handbook of Chemistry and Physics*, 59th edn. (CRC, Boca Raton 1978)

21.3   J. Borenstein, H.R. Everett, L. Feng: *Navigating Mobile Robots* (Peters, Wellesley 1996)

21.4   R. Kuc, M.W. Siegel: Physically-based simulation model for acoustic sensor robot navigation, IEEE Trans. Pattern Anal. Mach. Intell. **9**(6), 766–778 (1987)

21.5   SensComp: *7000 Series* (SensComp, Livonia 2007), http://www.senscomp.com

21.6   H.H. Poole: *Fundamentals of Robotics Engineering* (Van Nostrand, New York 1989)

21.7   J.E. Piercy: *American National Standard: Method for Calculation of the Absorption of Sound by the Atmosphere ANSI SI-26-1978* (Acoust. Soc. Am., Washington 1978)

21.8   B. Barshan, R. Kuc: A bat-like sonar system for obstacle localization, IEEE Trans. Syst. Man Cybern. **22**(4), 636–646 (1992)

21.9   R. Kuc: Three dimensional docking using qualitative sonar. In: *Intelligent Autonomous Systems IAS-3*, ed. by F.C.A. Groen, S. Hirose, C.E. Thorpe (IOS, Washington 1993) pp. 480–488

21.10   R. Kuc: Biomimetic sonar locates and recognizes objects, J. Ocean. Eng. **22**(4), 616–624 (1997)

21.11   L. Kleeman, R. Kuc: Mobile robot sonar for target localization and classification, Int. J. Robot. Res. **14**(4), 295–318 (1995)

21.12   B. Stanley: A comparison of binaural ultrasonic sensing systems. Ph.D. Thesis (University of Wollongong, Wollongong 2003), http://adt.caul.edu.au/

21.13   F.L. Degertekin, S. Calmes, B.T. Khuri-Yakub, X. Jin, I. Ladabaum: Fabrication and characterization of surface micromachined capacitive ultrasonic immersion transducers, J. Microelectromech. Syst. **8**(1), 100–114 (1999)

21.14   B. Barshan, R. Kuc: Differentiating sonar reflections from corners and planes by employing an intelligent sensor, IEEE Trans. Pattern Anal. Mach. Intell. **12**(6), 560–569 (1990)

21.15   A. Freedman: A mechanism of acoustic echo formation, Acustica **12**, 10–21 (1962)

21.16   A. Freedman: The high frequency echo structure of somae simple body shapes, Acustica **12**, 61–70 (1962)

21.17   Ö. Bozma, R. Kuc: A physical model-based analysis of heterogeneous environments using sonar – ENDURA method, IEEE Trans. Pattern Anal. Mach. Intell. **16**(5), 497–506 (1994)

21.18   Ö. Bozma, R. Kuc: Characterizing pulses reflected from rough surfaces using ultrasound, J. Acoust. Soc. Am. **89**(6), 2519–2531 (1991)

21.19   P.J. McKerrow: Echolocation – from range to outline segments. In: *Intelligent Autonomous Systems IAS-3*, ed. by F.C.A. Groen, S. Hirose, C.E. Thorpe (IOS, Washington 1993) pp. 238–247

21.20   J. Thomas, C. Moss, M. Vater (Eds.): *Echolocation in Bats and Dolphins* (University of Chicago Press, Chicago 2004)

21.21   J. Borenstein, Y. Koren: Error eliminating rapid ultrasonic firing for mobile robot obstacle avoidance, IEEE Trans. Robot. Autom. **11**(1), 132–138 (1995)

21.22   L. Kleeman: Fast and accurate sonar trackers using double pulse coding, Proc. IEEE/RSJ Int. Conf. Intell. Robot. Syst. (1999) pp. 1185–1190

21.23   R. Kuc: Pseudo-amplitude sonar maps, IEEE Trans. Robot. Autom. **17**(5), 767–770 (2001)

21.24   H. Peremans, K. Audenaert, J.M. Van Campenhout: A high-resolution sensor based on tri-aural perception, IEEE Trans. Robot. Autom. **9**(1), 36–48 (1993)

21.25   A. Sabatini, O. Di Benedetto: Towards a robust methodology for mobile robot localization using sonar, IEEE Int. Conf. Robot. Autom. (1994) pp. 3136–3141

21.26   L. Kleeman: Advanced sonar with velocity compensation, Int. J. Robot. Res. **23**(2), 111–126 (2004)

21.27   A. Elfes: Sonar-based real world mapping and navigation, IEEE Trans. Robot. Autom. **3**, 249–265 (1987)

21.28   S. Thrun, M. Bennewitz, W. Burgard, A.B. Cremers, F. Dellaert, D. Fox, D. Haehnel, C. Rosenberg,

N. Roy, J. Schulte, D. Schulz: MINERVA: A second geration mobile tour-guide robot, IEEE Int. Conf. Robot. Autom. (1999) pp. 3136–3141

21.29   K. Konolige: Improved occupancy grids for map building, Auton. Robot. **4**, 351–367 (1997)

21.30   R. Grabowski, P. Khosla, H. Choset: An enhanced occupancy map for exploration via pose separation, Proc. IEEE/RSJ Int. Conf. Intell. Robot. Syst. (2003) pp. 705–710

21.31   J.D. Tardos, J. Neira, P.M. Newman, J.J. Leonard: Robust mapping and localization in indoor environments using sonar data, Int. J. Robot. Res. **21**(6), 311–330 (2002)

21.32   O. Aycard, P. Larouche, F. Charpillet: Mobile robot localization in dynamic environments using places recognition, Proc. IEEE Int. Conf. Robot. Autom. (1998) pp. 3135–3140

21.33   B. Kuipers, P. Beeson: Bootstrap learning for place recognition, Proc. 18-th Nat. Conf. Artif. Intell. (AAAI-02) (2002)

21.34   A. Bandera, C. Urdiales, F. Sandoval: Autonomous global localization using Markov chains and optimized sonar landmarks, Proc. IEEE/RSJ Int. Conf. Intell. Robot. Syst. (2000) pp. 288–293

21.35   R. Kuc: Biomimetic sonar and neuromorphic processing eliminate reverberation artifacts, IEEE Sens. J. **7**(3), 361–369 (2007)

21.36   A.M. Sabatini: A stochastic model of the time-of-flight noise in airborne sonar ranging systems, IEEE Trans. Ultrason. Ferroelectr. Freq. Control **44**(3), 606–614 (1997)

21.37   C. Biber, S. Ellin, E. Sheck, J. Stempeck: The Polaroid ultrasonic ranging system, Proc. 67th Audio Eng. Soc. Convention (1990)

21.38   R. Kuc: Forward model for sonar maps produced with the Polaroid ranging module, IEEE Trans. Robot. Autom. **19**(2), 358–362 (2003)

21.39   M.K. Brown: Feature extraction techniques for recognizing solid objects with an ultrasonic range sensor, IEEE J. Robot. Autom. **RA-1**(4), 191–205 (1985)

21.40   N.L. Harper, P.J. McKerrow: Classification of plant species from CTFM ultrasonic range data using a neural network, Proc. IEEE Int. Conf. Neural Netw. (1995) pp. 2348–2352

21.41   Z. Politis, P.J. Probert: Target localization and identification using CTFM sonar imaging: The AURBIT method, Proc. IEEE Int. Symp. CIRA (1999) pp. 256–261

21.42   R. Mueller, R. Kuc: Foliage echoes: A probe into the ecological acoustics of bat echolocation, J. Acoust. Soc. Am. **108**(2), 836–845 (2000)

21.43   P.N.T. Wells: *Biomedical Ultrasonics* (Academic, New York 1977)

21.44   J.L. Prince, J.M. Links: *Medical Imaging Signals and Systems* (Pearson Prentice Hall, Upper Saddle River 2006)

21.45   J.J. Leonard, H.F. Durrant-Whyte: Mobile robot localization by tracking geometric beacons, IEEE Trans. Robot. Autom. **7**(3), 376–382 (1991)

21.46   P.M. Woodward: *Probability and Information Theory with Applications to Radar*, 2nd edn. (Pergamon, Oxford 1964)

21.47   A. Heale, L. Kleeman: Fast target classification using sonar, IEEE/RSJ Int. Conf. Robot. Syst. (2001) pp. 1446–1451

21.48   S. Fazli, L. Kleeman: A real time advanced sonar ring with simultaneous firing, Proc. IEEE/RSJ Intern. Conf. Intell. Robot. Syst. (2004) pp. 1872–1877

21.49   T. Yata, A. Ohya, S. Yuta: A fast and accurate sonar-ring sensor for a mobile robot, Proc. IEEE Int. Conf. Robot. Autom. (1999) pp. 630–636

21.50   L. Kleeman: Scanned monocular sonar and the doorway problem, Proc. IEEE/RSJ Int. Conf. Intell. Robot. Syst. (1996) pp. 96–103

21.51   G. Kao, P. Probert: Feature extraction from a broadband sonar sensor for mapping structured environments efficiently, Int. J. Robot. Res. **19**(10), 895–913 (2000)

21.52   B. Stanley, P. McKerrow: Measuring range and bearing with a binaural ultrasonic sensor, IEEE/RSJ Int. Conf. Intell. Robot. Syst. (1997) pp. 565–571

21.53   P.T. Gough, A. de Roos, M.J. Cusdin: Continuous transmission FM sonar with one octave bandwidth and no blind time. In: *Autonomous Robot Vehicles*, ed. by I.J. Cox, G.T. Wilfong (Springer-Verlag, Berlin, Heidelberg 1990) pp. 117–122

21.54   L. Kay: A CTFM acoustic spatial sensing technology: its use by blind persons and robots, Sens. Rev. **19**(3), 195–201 (1999)

21.55   L. Kay: Auditory perception and its relation to ultrasonic blind guidance aids, J. Br. Inst. Radio Eng. **24**, 309–319 (1962)

21.56   P.J. McKerrow, N.L. Harper: Recognizing leafy plants with in-air sonar, IEEE Sens. **1**(4), 245–255 (2001)

21.57   K. Audenaert, H. Peremans, Y. Kawahara, J. Van Campenhout: Accurate ranging of multiple objects using ultrasonic sensors, Proc. IEEE Int. Conf. Robot. Autom. (1992) pp. 1733–1738

21.58   J. Borenstein, Y. Koren: Noise rejection for ultrasonic sensors in mobile robot applications, Proc. IEEE Int. Conf. Robot. Autom. (1992) pp. 1727–1732

21.59   K.W. Jorg, M. Berg: Mobile robot sonar sensing with pseudo-random codes, Proc. IEEE Int. Conf. Robot. Autom. (1998) pp. 2807–2812

21.60   S. Shoval, J. Borenstein: Using coded signals to benefit from ultrasonic sensor crosstalk in mobile robot obstacle avoidance, Proc. IEEE Int. Conf. Robot. Autom. (2001) pp. 2879–2884

21.61   K. Nakahira, T. Kodama, T. Furuhashi, H. Maeda: Design of digital polarity correlators in a multiple-

user sonar ranging system, IEEE Trans. Instrum. Meas. **54**(1), 305–310 (2005)

21.62 A. Heale, L. Kleeman: A sonar sensor with random double pulse coding, Aust. Conf. Robot. Autom. (2000) pp. 81–86

21.63 A. Diosi, G. Taylor, L. Kleeman: Interactive SLAM using Laser and Advanced Sonar, Proc. IEEE Int. Conf. Robot. Autom. (2005) pp. 1115–1120

21.64 S.A. Walter: The sonar ring: obstacle detection for a mobile robot, Proc. IEEE Int. Conf. Robot. Autom. (1987) pp. 1574–1578

21.65 S. Fazli, L. Kleeman: Wall following and obstacle avoidance results from a multi-DSP sonar ring on a mobile robot, Proc. IEEE Int. Conf. Mechatron. Autom. (2005) pp. 432–436

21.66 S. Fazli, L. Kleeman: Sensor design and signal processing for an advanced sonar ring, Robotica **24**(4), 433–446 (2006)

21.67 W.W.L. Au: *The Sonar of Dolphins* (Springer-Verlag, Berlin, Heidelberg 1993)

21.68 B. Barshan, R. Kuc: Bat-like sonar system strategies for mobile robots, Proc. IEEE Int. Conf. Syst. Man Cybern. (1991)

21.69 R. Kuc: Biologically motivated adaptive sonar, J. Acoust. Soc. Am. **100**(3), 1849–1854 (1996)

21.70 V.A. Walker, H. Peremans, J.C.T. Hallam: One tone, two ears, three dimensions: A robotic investigation of pinnae movements used by rhinolophid and hipposiderid bats, J. Acoust. Soc. Am. **104**, 569–579 (1998)

21.71 R. Kuc: Biomimetic sonar system recognizes objects using binaural information, J. Acoust. Soc. Am. **102**(2), 689–696 (1997)

21.72 R. Kuc: Recognizing retro-reflectors with an obliquely-oriented multi-point sonar and acoustic flow, Int. J. Robot. Res. **22**(2), 129–145 (2003)

21.73 R. Mueller, R. Kuc: Foliage echoes: A probe into the ecological acoustics of bat echolocation, J. Acoust. Soc. Am. **108**(2), 836–845 (2000)

21.74 T. Horiuchi, T. Swindell, D. Sander, P. Abshire: A low-power CMOS neural amplifier with amplitude measurements for spike sorting, ISCAS, Vol. IV (2004) pp. 29–32

21.75 R. Kuc: Neuromorphic processing of moving sonar data for estimating passing range, IEEE Sens. J. – Special Issue on Intelligent Sensors **7**(5), 851–859 (2007)

Part C | 21